Invisible gold in arsenian pyrite and arsenopyrite from a multistage Archaean gold deposit: Sunrise Dam, Eastern Goldfields Province, Western Australia

Y.-H. Sung · J. Brugger · C. L. Ciobanu · A. Pring · W. Skinner · M. Nugus

Abstract The Sunrise Dam gold mine (11.1 Moz Au) is the largest deposit in the Archaean Laverton Greenstone Belt (Eastern Goldfields Province, Yilgarn Craton, Western Australia). The deposit is characterized by multiple events of fluid flow leading to repeated alteration and mineralization next to a major crustal-scale structure. The Au content of arsenian pyrite and arsenopyrite from four mineralizing stages (D_1, D_3, D_{4a}, and D_{4b}) and from different structural and lithostratigraphic environments was measured using in situ laser ablation inductively coupled plasma mass spectrometry. Pyrite contains up to 3,067 ppm Au ($n=224$), whereas arsenopyrite contains up to 5,767 ppm ($n=19$). Gold in arsenopyrite (D_{4a} stage) was coprecipitated and remained as "invisible gold" (nanoparticles and/or lattice-bound) during subsequent deformation events. In contrast, gold in pyrite is present not only as "invisible gold" but also as micrometer-size inclusions of native gold, electrum, and Au(Ag)–tellurides. Pristine D_1 and D_3 arsenian pyrite contains relatively low Au concentrations (≤26 ppm). The highest Au concentrations occur in D_{4a} arsenian-rich pyrite that has recrystallized from D_3 pyrite. Textures show that this recrystallization proceeded via a *coupled* dissolution–reprecipitation process, and this process may have contributed to upgrading Au grades during D_{4a}. In contrast, Au in D_{4b} pyrite shows grain-scale redistribution of "invisible" gold resulting in the formation of micrometer-scale inclusions of Au minerals. The speciation of Au at Sunrise Dam and the exceptional size of the deposit at province scale result from multiple fluid flow and multiple Au-precipitating mechanisms within a single plumbing system.

Keywords Sunrise Dam Gold Deposit, Eastern Goldfields Province, Western Australia · Pyrite · Arsenopyrite · Invisible gold

Y.-H. Sung · W. Skinner
Ian Wark Research Institute, University of South Australia,
Mawson Lakes, South Australia 5095, Australia

Y.-H. Sung · J. Brugger · C. L. Ciobanu · A. Pring
Division of Minerals, South Australian Museum,
Adelaide, South Australia 5000, Australia

J. Brugger (✉) · C. L. Ciobanu · A. Pring
School of Earth and Environmental Sciences,
University of Adelaide,
Adelaide, South Australia 5000, Australia
e-mail: joel.brugger@adelaide.edu.au

M. Nugus
Sunrise Dam Gold Mine, AngloGold Ashanti Australia Ltd,
Laverton, Western Australia 6001, Australia

Present Address:
Y.-H. Sung
Korea Resources Corporation,
79 Siheung daero, Dangjak-gu,
Seoul 156-706, South Korea

Introduction

Over the past decade, the Laverton Greenstone Belt (LGB) in the Eastern Goldfields Province of the Yilgarn Craton, Western Australia (Fig. 1) has become a major center of gold production with a total Au endowment of over 700 t Au (Salier et al. 2005). The belt contains two world-class deposits (>100 t Au), Sunrise Dam and Wallaby. The Sunrise Dam orogenic gold deposit is located approximately 850 km ENE of Perth and 45 km SSE of Laverton at 290°5′ S, 122°25′ E. With a total production by March 2007 of approximately 5.4 Moz Au and remaining

resources + reserves of 5.58 Moz Au, the mine is the single largest deposit in the LGB.

From the perspective of mineral processing, gold ores can be broadly classified as free milling (over 90% recovery) and refractory (less than 90% recovery; Vaughan 2004). Refractory gold ores have long been recognized from a range of Au deposits with different geological environments, genetic histories, and ages (e.g., Fleet et al. 1993; Fleet and Mumin 1997; Cabri et al. 1989; Cathelineau et al. 1989; Cook and Chryssoulis 1990; Arehart et al. 1993; Oberthür et al. 1997; Tarnocai et al. 1997; Genkin et al. 1998; Ashley et al. 2000; Simon et al. 1999a, b; Pals et al. 2003; Ciobanu et al. 2009). Submicroscopic or "invisible" (less than 0.1 μm) Au is by far the most common reason for refractory behavior, although low Au recovery may also be caused by other factors, e.g., the presence of Au(Ag)–tellurides (e.g., Kalgoorlie, Western Australia; Shackleton et al. 2003), or of fine-grained inclusions of native gold (less than 10 μm) within sulfides.

The Sunrise Dam deposit has a complex tectonic evolution leading to a protracted history of Au deposition and remobilization (Nugus et al. 2005a, b). Although the deposit is generally regarded as low-sulfide type (Brown et al. 2002), Au occurs as native gold inclusions in sulfides/sulfosalts and also forms Au(Ag)–tellurides (Sung et al. 2007). The deposit contains both free-milling and refractory Au ores, and the average Au recovery is about 80%. The refractory Au ores at Sunrise Dam consist mainly of arsenian pyrite and arsenopyrite.

Consequently, a laser ablation inductively coupled plasma mass spectrometry (LA-ICP-MS) study has been conducted on pyrite and arsenopyrite to evaluate the concentration and the nature of refractory Au in the deposit. This study provides the basic information about the nature of invisible gold necessary to understand the relatively low gold recovery rate. Combined with petrological observations, the LA-ICP-MS data enable us to discuss aspects of gold deposition and remobilization during the successive deformational stages and via different precipitation mechanisms. Lastly, this should provide an insight into the various mechanisms of Au enrichment in a world-class orogenic Au deposit.

The Sunrise Dam deposit

The Sunrise Dam deposit is located in the Archaean Laverton Tectonic Zone (LTZ), occupying the highly deformed central domain of the LGB (Fig. 1). The majority of the LTZ has undergone metamorphism at lower greenschist facies conditions (Hallberg 1985). The lithologies in the mine area comprise an intermediate volcanoclastic sequence that dips gently to the NW and is overlain by turbidite sedimentary rocks, the latter one of which
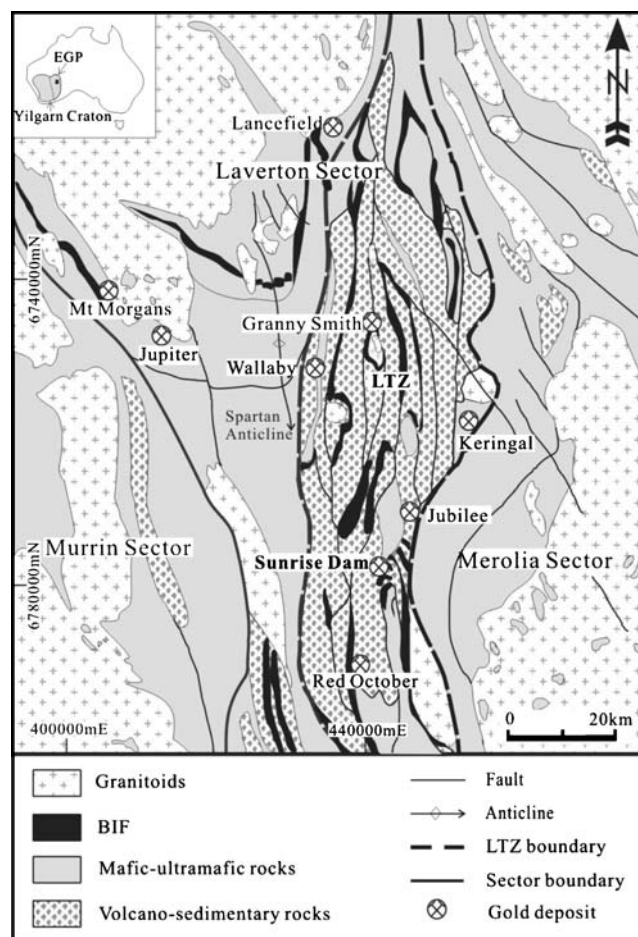

Fig. 1 Simplified geological map of the Laverton Greenstone Belt (modified after Salier et al. 2005), showing the sectors suggested by Cassidy et al. (2002) and the position of Laverton Tectonic Zone (*LTZ*) that hosts the majority of gold deposits in this area, including Sunrise Dam. *Inset*: position of the area shown in the map (*rectangle*) in the Yilgarn Craton and Eastern Goldfield Province (*EGP*)

includes banded iron formation (BIF) sequences (magnetite-rich shales and cherts; Fig. 2). Dikes and sills of dolerite and ultramafic rocks intrude the sedimentary rocks, whereas rhyodacite porphyry intrudes any lithological unit.

Structures and orebodies

Gold mineralization occurs intermittently along a NE-trending corridor of ca. 4.5 km length, characterized by the presence of strongly magnetic BIF sequences (Newton et al. 2002). The 20 currently defined orebodies are centered onto a series of parallel, gently dipping (~30°), and NE-trending shear zones with a thrust-duplex architecture and high-strain character. These shear zones are, from west to east, Cleo Upper Shear (CUS), Sunrise Shear Zone (SSZ), and Carey Shear (CS; Fig. 2). Such gentle-dipping structures, characteristic of many orogenic gold deposits in the LGB (e.g., Wallaby, Granny Smith, Lancefield, Jubilee),

Fig. 2 Plan view of major lithologies and structures in the Sunrise Dam gold deposit showing projected locations of LA-ICP-MS samples. *1* GQ 1960 OD, *2* GQ open pit 67.5 RL, *3* Astro UGD 728, *4* Mako 2087 OD, *5* SSZ 2075 OD, *6* SSZ 2077 OD, *7* SSZ 2067 OD, *8* SSZ open pit W-wall, *9* Cosmo 1940 OD, *10* Dolly Volcanic 1931 OD, *11* Dolly Porphyry 1930 OD, *12* Margies open pit S-wall, *13* WSZ 2109 OD, *14* WSZ open pit S-wall, *15* WFZ open pit SE-wall, *CUS* Cleo Upper Shear, *SSZ* Sunrise Shear Zone, *CS* Carey Shear, *WSZ* Western Shear Zone, *WFZ* Watu Fault Zone. Mine grid is rotated 45° E of true north
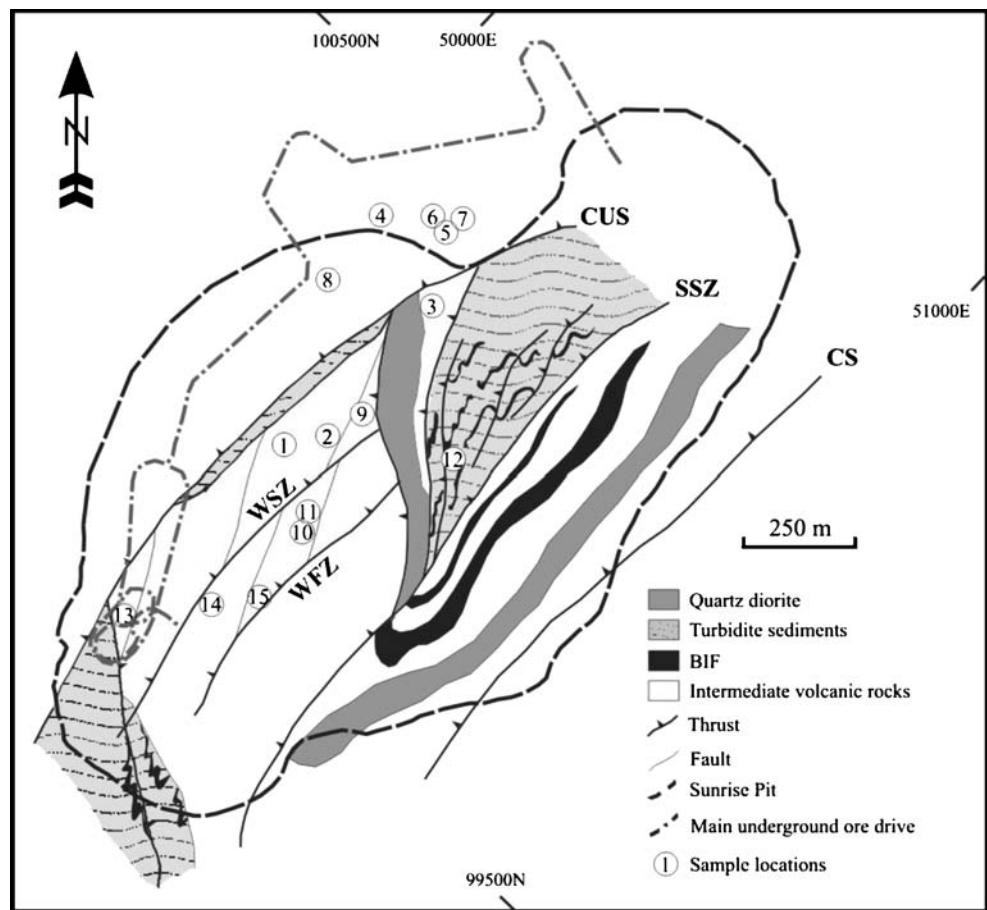
usually carry a significant proportion of the ore. At Sunrise Dam, the SSZ alone hosts in excess of 1.5 of the 11 Moz Au contained in the whole deposit (Nugus et al. 2005a).

A number of orebodies in the deposit are hosted within steep shear zones, e.g., Western Shear Zone (WSZ) and Watu Fault Zone (WFZ) that in turn are located between the gently dipping CUS and the SSZ (Fig. 2). These lodes carry higher and more consistent grades (Au at 15 g/t in WSZ; Au at 13 g/t in WFZ) than those hosted by the SSZ.

All the above structures are NE-trending and contain ~80% of the Au resource whereas the rest is hosted by N–S shears, e.g., Summer Cloud, Predator, Hammer Head, and Cosmo orebodies. These contain an important part of the 1.71-Moz current underground resource (0.55 Moz at 8.96 g/t Au; Nugus et al. 2005a).

Gold deposition and deformation history

Four major deformational stages are currently recognized at Sunrise Dam. The earliest deformation (D_1) formed F_1 folds and thrusts (i.e., SSZ, CUS, and CS) in response to N–S compression and shortening (S_1; Nugus et al. 2005a). The second event (D_2) was characterized by regional E–W shortening associated with the formation of the regional Spartan Anticline (F_2 fold; see Fig. 1) and penetrative N–S

trending cleavage (S_2). These two deformational stages were associated with hydrothermal alteration of country rocks (carbonate–chlorite–sericite) and only minor low-grade Au mineralization (generally <1 g/t). The two following stages, D_3 and D_4, are responsible for the bulk of the mineralization. D_3 produced major shear and/or fault zones such as WSZ and WFZ as a result of deformation caused by NNW–SSE to NW–SE oriented stress. This was also responsible for reactivation of S_1 and S_2 with sinistral strike-slip movement, as well as development of mineralized S_3 fractures and NE-trending extensional vein arrays. The last deformational event (D_4) resulted from NW–SE shortening with local dextral reactivation on S_3 surfaces and produced extensional Au lodes. The D_4 veins can be subdivided into steeper-dipping, early (D_{4a}), and gentle-dipping late veins (D_{4b}); D_{4b} veins crosscut the D_{4a} veins.

The D_3 and D_4 veins differ in terms of mineralogy, texture, and geochemical signatures. The vein filling consists mainly of quartz and carbonates in various proportions; quartz dominates in the D_{4b} veins. Pyrite is the main ore mineral present in all veins, arsenopyrite is particularly rich in D_{4a}, whereas base-metal sulfides and Pb–Sb sulfosalts are mainly found in the D_{4b} veins. Tellurides are present in both types of D_4 veins, but

particularly abundant and diverse in D_{4b} veins (Sung et al. 2007). Coarse native gold is common in D_{4a} veins. Replacement of BIF by pyrite during faulting in the D_3 stage is another common aspect (e.g., Fig. 3a). Evidences of overlap between the D_4 and D_3 stages are widespread. For example, two types of veins are recognizable in Fig. 3b: (a) a thin, white, isoclinically folded D_3 vein and (b) a thicker D_{4a} vein consisting of laminated gray quartz; the gray color is due to fine-grained arsenopyrite. Characteristic of the D_4 veins are dark internal laminae (Fig. 3c). In detail, such laminae may have a stylolitic aspect and complex mineralogy, e.g., muscovite, tourmaline, apatite, rutile, as well as pyrite and minor native gold and tellurides. Post-D_4 deformation is also recognizable as oblique laminae crosscutting the internal fabric of the D_4 veins, e.g., Fig. 3d. It is on such internal structures that local-scale remobilization can lead to formation of the most diverse telluride assemblages (Sung et al. 2007).

Country-rock alteration is similar in both D_3 and D_4 stages. Importantly, this is always associated with dissemination of fine-grained pyrite and arsenopyrite. The most intense alteration is sericite + ankerite/dolomite adjacent to veins, whereas distal alteration includes mainly chlorite + calcite. Chromium-bearing mica ("fuchsite") is present preferentially in the central part of the deposit below the SSZ (e.g., SSZ, GQ, and Cosmo orebodies) and is usually associated with Cr-rich mafic dikes and sills and mafic volcanogenic lithofacies.

The geochronological framework established by Brown et al. (2002) indicates that the D_3 and D_4 mineralizations occurred in the interval ~2,670–2,650 Ma. Intrusion of rhyodacite porphyry at 2,674±3 Ma (SHRIMP II U–Pb on zircons) predates the formation of D_4 veins (corresponding to D_3 in the nomenclature of Brown et al. 2002). This age overlaps with the 2,663±11 Ma Re–Os age obtained on D_1 molybenite in quartz veins crosscutting the porphyry.
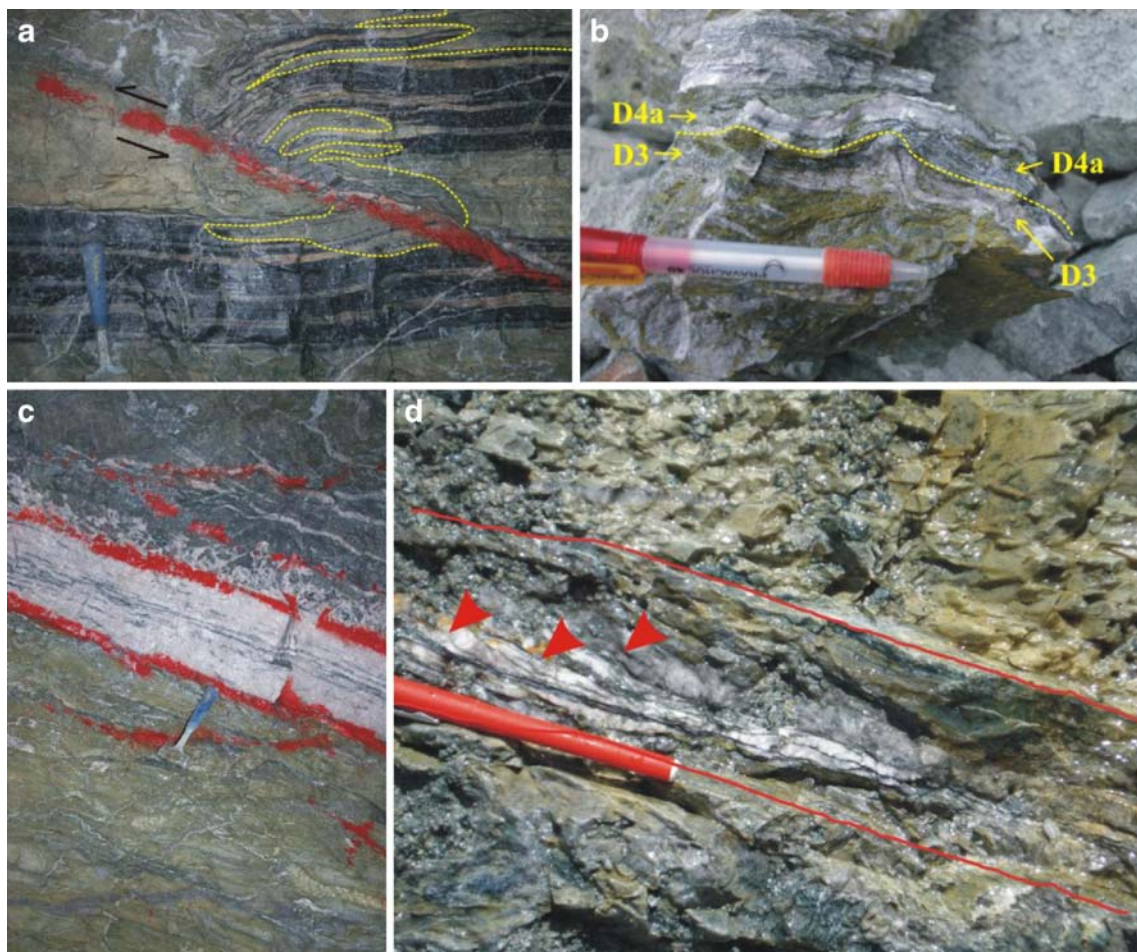
Fig. 3 Mineralization styles in the Sunrise Dam mine. **a** Sulfidation of BIF (outlined by *dotted lines*) along a fault plane; 2067 ore drive, SSZ. **b** Laminated D_{4a} vein crosscutting folded D_3 vein, WSZ open pit. Note more highly deformed and bleached appearance of D_3 veins. **c** Typical high-grade D_{4b} vein showing stylolitic laminae. The numerous quartz veins in the host rock belong to the D_3 and D_{4a} stages. Also note the collocation of the D_{4b} vein with a subparallel breccia zone on the top. 2066 ore drive, SSZ. **d** Post-D_4 laminae affecting a D_{4b} vein

Brown et al. (2002) consider that the main stage mineralization is constrained by a 2,667±3 Ma age from $^{40}Ar/^{39}Ar$ dating of Cr-mica from the SSZ and a 2,654±8 Ma SHRIMP II U–Pb age on hydrothermal xenotime and monazite from the WSZ.

Fluid sources and gold deposition mechanisms

Fluid inclusion data on samples from gently (SSZ) and steeply dipping (WSZ; "Western Lodes" in Brown et al. 2003) orebodies indicate that the chemistry of Au-bearing fluids was identical (Brown et al. 2003). The mineralization is considered to be formed from a CO_2–H_2O dominant, moderate-salinity fluid (6–9 wt.% NaCl equivalent) with homogenization temperatures ranging from 280°C to 320°C. Assuming no posttrapping inclusion modification, Brown et al. (2003) estimated trapping pressures of 80–130 MPa from isochores at 280°C, corresponding to a depth of formation of ~4 km under transient hydrostatic pressure. Based on variations in H_2O/CO_2 ratios among secondary inclusions with homogenization temperatures similar to the main fluid, Brown et al. (2003) suggest that Au deposition in the WSZ lodes may be related to intermittent phase separation, whereas for SSZ, precipitation of Au was mainly triggered by wall rock sulfidation of BIF units.

Samples selection, preparation, and analytical techniques

Representative ore samples were collected from ten orebodies (Table 1; Fig. 2), and a total of 138 polished blocks were prepared and examined under a Leitz Laborlux-12-Pol dual reflected–transmitted light polarizing microscope and Philips XL30 scanning electron microscopy (SEM) with energy dispersive X-ray spectrometry and back-scattered electron (BSE) imaging capabilities. Native gold (including electrum), pyrite, and arsenopyrite were analyzed with a CAMECA SX-51 electron microprobe (EMP) with wavelength dispersion spectrometers at Adelaide Microscopy Centre, University of Adelaide, Australia. The measurements were performed at 20 kV with a beam current of 19.5 nA, using the following X-ray lines and standards: Fe$K\alpha$ (CuFeS$_2$), S$K\alpha$ (PbS), As$K\alpha$ (CoAsS), Sb$L\alpha$ (Sb$_2$S$_3$), and Au$L\alpha$ (Au).

A total of 260 LA-ICP-MS spot analyses were performed on 38 polished blocks representing different paragenetic stages and orebodies (Table 1). The analyses were carried out using an Agilent HP 4500 ICP-MS with a New Wave UP-213 Nd:YAG laser ablation system at CODES, University of Tasmania, Australia. Single-spot analyses were performed with a laser beam diameter between 20 and 40 μm, depending on the size of ablated mineral. The CODES standard STDGL2b-2 was used as primary standard in this study. It consists of powdered sulfides doped with certified element solutions and fused with lithium borate into a glass disc (Danyushevsky et al. 2003). Fe concentrations were used as internal standard. Data were collected during 100 s, including an initial 30 s of the carrier gas background before the laser was switched on. A total of 11 elements were monitored: ^{53}Cr, ^{59}Co, ^{60}Ni, ^{65}Cu, ^{75}As, ^{107}Ag, ^{121}Sb, ^{125}Te, ^{197}Au, ^{208}Pb, and ^{209}Bi. The lowest values of minimum detection limit are (in ppm): Cr 0.393, Co 0.025, Ni 0.066, Cu 0.331, As 0.369, Ag 0.038, Sb 0.022, Te 0.302, Au 0.014, and Pb 0.009. The integration ranges used for calculating concentrations were selected to avoid inhomogeneities and spikes likely related to buried inclusions; examples of integration intervals are shown in Fig. 4. A more detailed interpretation of time-resolved LA-ICP-MS spectra is given below in section "LA-ICP-MS spectra".

Composition of pyrite and arsenopyrite: results of LA-ICP-MS analyses

In this section, we summarize the concentrations and distribution of trace and minor elements in pyrite and arsenopyrite from the Sunrise Dam deposit, based mainly on LA-ICP-MS analyses. Sample location, mineralogy, stages, and host rocks are listed in Table 1. A summary of gold concentrations in pyrite from different stages is given in Table 2, all the data obtained for arsenopyrite are listed in Table 3, and the full dataset for pyrite is included in Appendix.

Gold and other trace elements in pyrite

The Au content of pyrite ranges from below detection limit (<0.014 ppm) up to 3,067 ppm, with an average of 1.61 ppm (based on 224 spot analyses; Table 2; Appendix). Unless noted otherwise, reported averages for trace elements in this paper were calculated on logarithmic concentrations, and analyses below detection limits were included at half the value of the detection limit. Histograms show that pyrite from each stage of mineralization has wide ranges in Au concentrations (Fig. 5). The few analyses of pyrite from D$_1$ (n=6; average 1.12 ppm, range <0.3 to 6.56 ppm) show similar contents as D$_3$ (n=53, average 0.56 ppm, range <0.04 to 25.8 ppm) and D$_{4b}$ (n=61, average 1.17 ppm, range <0.1 to 18.2 ppm). The D$_1$ dataset is limited because it is difficult to identify pristine D$_1$ pyrite. The average Au content for the D$_{4b}$ stage reduces to 0.89 ppm if three points (circled in Fig. 5) that contain an order of magnitude more Au (140–290 ppm) and Te (499–

Table 1 Sample locations and descriptions for the LA-ICP-MS analysis

| Sample number	Orebody	Location	Stage	Host rock	Ore minerals	
					Major	Minor
GQ1-1	GQ	Open pit 67.5RL	D4b	Ivr	Py	Tn, Apy
GQ1-2a			D4b		Py	Tn, Mt, Sch
GQ1-4			D3		Py	Tn
GQ1-6			D4a		Py, Apy	Cp, Tn, Au
GQ1-9			D3/D4a	BIF	Py	Hs
GQ1-10			D4b	Rdp	Py	Tn, Mo, Cp, Mt, Cst, Str
GQ1-13			D3	Ivr	Py	Tn, Au
GQ19		1960OD	D4a	Ivr	Py	Cp, Chr, Gdf, Au, Mel, Hs
A3	Astro	UGD728	D4a	BIF	Py	Cp, Tn, Au
A4			D4a	BIF	Py	Au, Tn, Apy
Mk2-1	Mako	2087OD	D4a	Ivr	Py	Cp
Mk2-2			D4b		Py	Gn, Au, Tn, Cal, Alt, Mel
S7-2	SSZ	Open pit W-wall	D1	?	Py	Tn, Mo, Cp
S311		2075OD	D3	BIF	Py	Cp, Mt, Tn
S313			D3		Py	Apy
SU17		2067OD	D3/D4a		Py	Apy, Mt
SU15			D4b	Ivr	Py	Sp, Cp, Hs
SU2		2077OD	D3		Py	
SU11			D3	BIF	Mt	He, Py, Cp, Sch
SU4			D4b	Ivr	Sp, Py	Cp, Gn, Au, Nag
SU10			D4b		Sp, Gn	Py, Cp, Tn, Nag, Au, Bnn
SU5			D4b		Py	Cp, Hs, Tn, Au
C4-2	Cosmo	1940OD	D3/D4a	Ivr	Py	Po, Cp, Apy
C4-6			D4a		Apy, Py	
Dv5-1	Dolly Volcanic	1931OD	D4a		Apy, Py	Tn
Dv5-2a			D4b		Py	
Dp6-1	Dolly Porphyry	1930OD	D4a	Rdp	Apy	Py
Dp6-2			D4a		Py	Mt
Mg8-1	Margies	Open pit S-wall	D3	Dlt	Py	Mo, Tn, Cp
Mg8-3			D4a		Py	Tn, Cp
Mg8-3b			D4a		Py	
Mg8-6			D4b		Py	Mo, Tn
Mg-1			D4b	Rdp	Py	
WSZ333	WSZ	Open pit S-wall	D4a	Ivr	Py, Apy	
WSZ-15			D4a		Py	Cp, Tn
WSZ6-7a		2109OD	D4a		Apy	Py
WFZ311	WFZ	Open pit SE-wall	D4a	Ivr	Py, Apy	Cp, Gn, Apy, Tn
WFZ312			D4a		Py, Apy	Cp, Po, Ttd

OD ore drive, *SSZ* Sunrise Shear Zone, *WSZ* Western Shear Zone, *WFZ* Watu Fault Zone, *Ivr* intermediate volcanic rock, *BIF* banded iron formation, *Rdp* rhyodacite porphyry, *Dlt* dolerite, *Alt*-altaite, *Ank* ankerite, *Apy* arsenopyrite, *Au* native gold, *Bnn* bournonite, *Chr* chromite, *Cp* chalcopyrite, *Cst* cassiterite, *Gdf* gersdorffite, *Gn* galena, *Hs* hessite, *Mel* melonite, *Mo* molybdenite, *Mt* magnetite, *Nag* nagyágite, *Pl* plagioclase, *Po* pyrrhotite, *Py* pyrite, *Qz* quartz, *Sch* scheelite, *Sp* sphalerite, *Str* strontianite, *Tn* tennantite–tetrahedrite, *Ttd* tetradymite

6,426 ppm) than the other 59 points (sample Mk2-2, Mako orebody) are excluded. Such high Au and Te contents are attributed to calaverite inclusions, an interpretation that is consistent with the abundance of telluride inclusions in this sample (Table 1). The D_{4a} stage shows a significantly wider range in Au concentrations than the other stages, resulting in higher average concentration ($n=104$, average 3.65 ppm, range <0.1 to 3,067 ppm). The highest value is an outlier and the mean becomes 3.42 ppm when this is excluded; this leaves the maximum value at 540 ppm.

Arsenic concentrations vary from 8 ppm to 6.7 wt.%, spanning nearly four orders of magnitude. The dataset does

not reveal any significant difference in As distribution from one stage to another (Fig. 5). The wedge-shaped plot obtained for Au vs. As concentration in pyrite (Fig. 6) is similar to that known for pyrite in Carlin and epithermal Au deposits (Reich et al. 2005). The pyrite from D_{4b} plots at the upper part of the wedge and includes the highest As and Au values.

Tellurium concentrations vary from <0.3 to 6,426 ppm, also spanning over four orders of magnitude (Figs. 5 and 7). As for Au, the highest Te contents are found in the D_{4a} and D_{4b} stages (Fig. 5), with D_{4a} showing the highest average Te concentration (8.17 ppm); the other stages have average
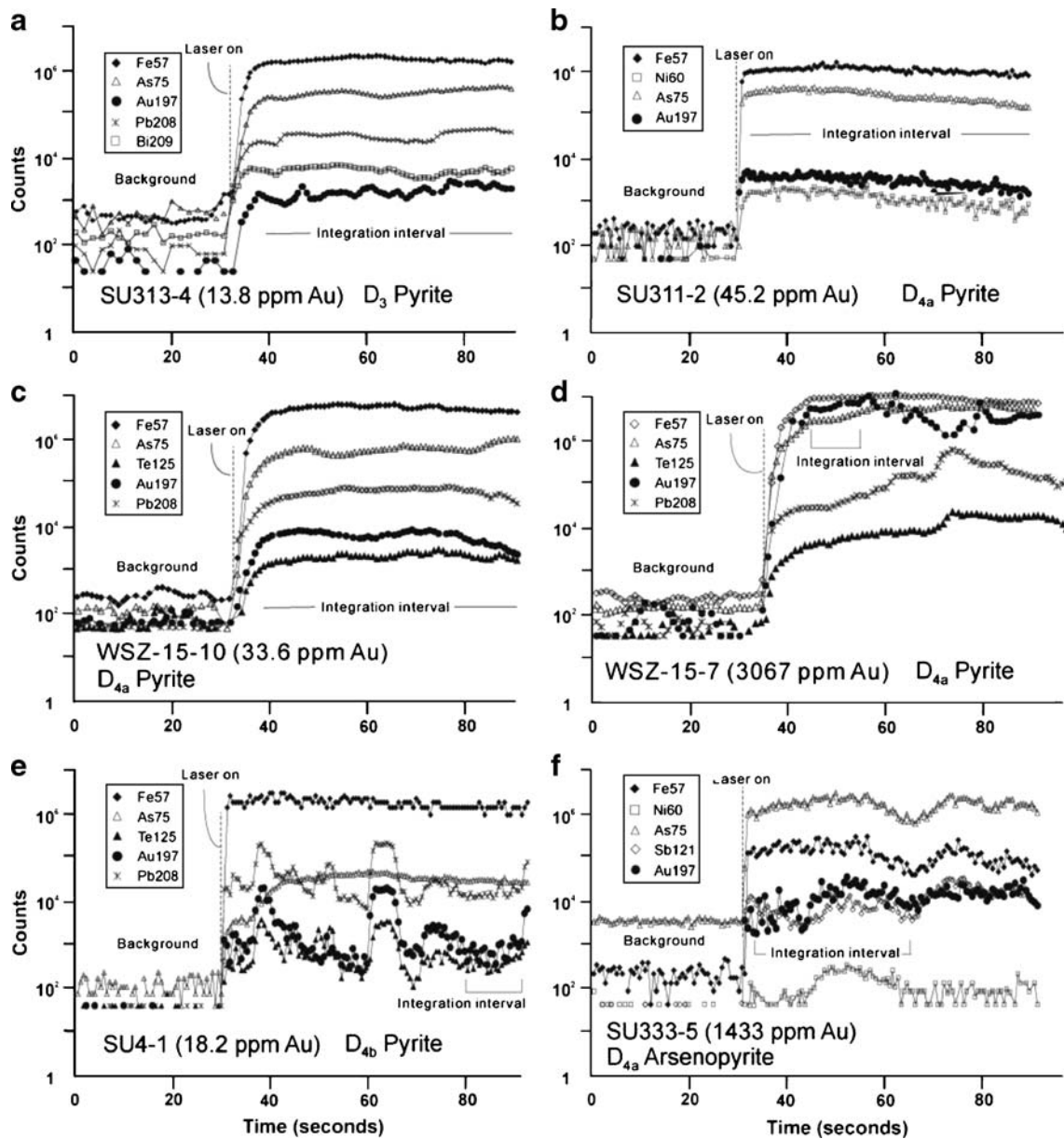
Fig. 4 Different types of LA-ICP-MS profiles obtained on Sunrise Dam pyrites (**a**–**e**) and arsenopyrite (**f**). The selected integration intervals for concentration calculations are also shown. **a** Pyrite crystal from the D_3 stage, showing smooth pattern for As and other trace elements, but a spikier pattern for Au, indicating the presence of suboptical gold particles. **b**, **c** Pyrite crystal from the D_{4a} stage (WSZ orebody) showing a relatively smooth and steady ablation profile for Au, attributed to invisible gold (i.e., Au in solid solution or as inclusion <0.1 μm). Note the positive correlation between the Au and As signals during the first 30 s of ablation in **c**. **d** D_{4a} stage pyrite

crystal (*WSZ*) displaying the highest Au concentration measured in this study, due at least in part to the presence of submicrometer gold inclusions. **e** Pyrite from the SSZ orebody (2077 ore drive) closely associated with nagyágite in a D_{4b} stage quartz vein. LA-ICP-MS traces reveal sharp variations in Au signal that are mimicked by the Te and Pb signals. This is characteristic for the presence of buried inclusions of nagyágite. **f** Arsenopyrite from the D_{4a} stage, showing inhomogeneous Ni distribution, but homogeneous Au distribution. Variations in Fe and As signals indicate the presence of quartz inclusion among the fine-grained arsenopyrite

Te concentrations at 4.41, 2.22, and 2.20 ppm for D_{4b}, D_3, and D_1, respectively. A broad positive correlation between Au and Te is revealed in Fig. 7b.

In addition, the following trace elements were also measured in pyrite: Ni (11.8 ppm to 2.0 wt.%), Co (2.1 ppm to 1.3 wt.%), Cr (<0.7 to 3,900 ppm), Cu (1.7 ppm to 4.7 wt.%), Ag (0.15 to 3,310 ppm), Sb (0.4 to

5,260 ppm), Pb (0.9 to 5,750 ppm), and Bi (0.05 to 2,180 ppm; Table 2). These elements also have wide ranges in concentration that span several orders of magnitude but in this case, there are no obvious differences among stages (Fig. 5; Appendix). Prominent correlations are observed between Ni and Co (Fig. 8a) and also among the elements Pb, Ag, Sb, and Bi (e.g., Pb vs. Bi in Fig. 8b).

Table 2 LA-ICP-MS analyses of pyrite in the Sunrise Dam gold deposit (data in parts per million)

Stage			Cr	Co	Ni	Cu	As	Ag	Sb	Te	Au	Pb	Bi
D_1	$n=6$	Min	<3.9	410	268	292	404	1.73	13.6	1.17	<0.3	49.9	36.4
		Max	61.3	3,245	1,458	46,633	15,099	43.4	1,959	4.07	6.56	1,040	261
		Mean (log)	14.0	1,129	599	1,984	1,529	12.5	255	2.20	1.12	139	93.1
		Mean (raw)	25.1	1,446	694	9,167	3,611	18.1	652	2.42	2.42	255	113
D_3	$n=53$	Min	<0.9	<0.8	4.77	1.13	8.06	<0.04	<0.02	<0.24	<0.01	0.08	<0.01
		Max	165	12,725	19,610	35,783	27,298	3,310	3,106	92.8	25.8	761	236
		Mean (log)	4.41	79.0	258	54.2	1,109	0.98	3.68	2.22	0.56	12.1	2.37
		Mean (raw)	14.2	516	913	1,340	5,605	65.6	113	7.51	2.36	76.3	21.1
D_{4a}	$n=104$	Min	<0.6	<0.1	<0.7	0.54	29	<0.04	0.02	<0.2	<0.01	<0.01	<0.004
		Max	3,924	5,606	25,699	13,653	66,819	1,564	2,736	538	3,067	6,090	2,180
		Mean (log)	6.21	103	430	86.7	2,559	1.71	9.62	8.17	3.65	34.7	4.58
		Mean (raw)[a]	87.0	377	1,160	1,081	8,465	15.0	132	43.1	41.6	253	86.7
D_{4b}	$n=61$	Min	0.74	<0.03	1.27	<0.6	15.5	<0.04	<0.02	<0.4	<0.01	<0.01	<0.004
		Max	439	15,640	2,858	27,296	19,534	568	5,256	6,426	290	5,751	110
		Mean (log)	2.53	27.6	159	27	1,540	0.52	2.27	5.41	1.17	6.65	1.01
		Mean (raw)[b]	19.2	422	489	997	4,026	14.9	232	12.2	3.34	71.9	11.1
Average	$n=224$	(Log)	4.57	71.1	287	60.6	1,776	1.10	5.58	5.10	1.61	17.4	2.74
	$n=220$	(Raw)	49.9	452	910	1,341	6,473	27.3	168	25.2	21.0	163	51.7

Means based on both logarithmic and raw values are shown. Analyses below detection limits (DL) were included at DL/2 value

[a] Outlier WSZ-15-7 omitted

[b] Three outliers (cf. Fig. 5) were omitted

In contrast, there is no correlation between Ni and Cr (Fig. 8c).

Gold and other trace elements in arsenopyrite

Arsenopyrite is a major ore mineral in the D_{4a} stage and it occurs mainly in the central and deeper part of the deposit, e.g., WSZ, WFZ, Astro, Cosmo, Dolly Volcanic, Dolly Porphyry, and GQ orebodies. Of these, the WSZ and Dolly Volcanic orebodies are particularly As-rich, containing approximately equal amounts of arsenopyrite and pyrite.

The LA-ICP-MS data show significantly higher values of Au in arsenopyrite (Table 3) compared to pyrite; concentrations range from 0.81 to 5,767 ppm Au with an average of 562 ppm Au. In contrast to pyrite, the histogram of Au concentration in arsenopyrite is skewed toward the higher concentrations (Fig. 5).

The Te concentrations vary from 6 ppm to 1.7 wt.% (Fig. 5); contrary to pyrite, there is no correlation between Te and Au, but instead, two distinct populations emerge (Fig. 7a). It appears that arsenopyrite from samples collected near porphyry intrusions forms a distinct population, higher in Te relatively to samples from the other orebodies. Arsenopyrite can also have high concentrations of Sb (to 1.7 wt.%), Ni (to 1.0 wt.%), and Pb (to 1.5 wt.%). The highest concentrations of Cr (288–1,853 ppm) were measured in arsenopyrite from Cosmo (other arsenopyrites

have ≤399 ppm), which also contains relatively high Co (307–473 ppm) and Ni (6,200–9,974 ppm; Table 3).

LA-ICP-MS spectra

Different types of time-resolved LA-ICP-MS profiles were obtained from pyrites (Fig. 4). Smooth and steady ablation profiles for Au, with a positive correlation between the Au and As signals, were obtained from most D_{4a} pyrites (Fig. 4b, c). This type of pattern is attributed to invisible gold, i.e., gold in solid solution or as inclusions <0.1 μm. We observe, however, that the correlation between the As and Au signals can change across the ablation interval (Fig. 4c). The Au signal in the richest auriferous pyrite (D_{4a}) is irregular, although it remains at relatively high level, whereas the As signal is smooth in comparison; parallel signals are obtained for Pb and Te in the same spectra (Fig. 4d). This type of pattern is interpreted as reflecting the presence of submicrometer gold inclusions, a fact confirmed by BSE images showing the presence of such native gold inclusions (<0.5 μm in size). Some of the D_3 pyrites have similar LA-ICP-MS profiles, although the Au concentrations are much lower (Fig. 4a).

Another type of spectra, characteristic of D_{4b} pyrite, but found in a few D_{4a} pyrite crystals as well, shows sharp variations in Au signal that are mimicked by the Te and Pb signals (Fig. 4e). This is interpreted as characteristic for the

Table 3 LA-ICP-MS analyses of arsenopyrite from different orebodies in the Sunrise Dam gold deposit (data in parts per million)

Spot no	Orebody	Occurrences	Cr	Co	Ni	Cu	Ag	Sb	Te	Au	Pb	Bi
apy-c-4-1	Astro	Euh	<37.4	19.9	132	104	<7.16	8,731	2,206	3,776	89.6	<2.95
apy-c-4-2		f-g, agg	<37.2	11.3	247	205	<6.68	4,645	17,730	5,280	451	7.07
apy-c-4-3		euh, agg	<27.4	75.0	472	1,701	18.4	2,101	4,483	2,657	454	7.33
apy-c-4-4		f-g, sub	333	45.6	290	148	<12.0	1,509	9,570	2,470	121	<5.50
Mean			35.5	29.6	258	271	6.03	3,367	6,400	3,382	217	3.81
apy-4-6-1	Cosmo	f-g, agg	1,853	473	9,974	690	116	1,663	2,685	223	1,799	217
apy-4-6-2			1,416	384	7,630	497	83.3	1,224	1,445	510	1,323	160
apy-4-6-3			288	307	6,702	160	50.9	1,316	1,617	239	870	73.7
apy-4-6-4			402	393	6,200	1,425	39.2	1,492	2,600	644	641	82.9
Mean			742	385	7,499	529	66.3	1,414	2,010	364	1,073	121
apy-5-1a-1	Dolly Volcanic	Euh	<5.30	46.4	78.3	21.0	<0.54	79.4	122	24.7	14.9	2.48
apy-5-1a-2			<5.52	35.1	189	57.3	1.80	106	35.1	69.0	27.6	11.5
apy-5-1a-3		c-g	<4.11	20.2	403	11.8	<0.48	91.9	138	0.81	1.74	1.09
apy-5-1a-4		Euh	<4.22	65.9	168	12.8	<0.45	109	31.7	43.4	2.33	1.22
apy-5-1a-5		Euh	<4.01	54.2	371	13.0	0.48	155	48.9	16.0	7.20	8.57
Mean			2.29	41.1	206	18.8	0.42	105	62.0	15.7	6.54	3.18
apy-6-1a-1	Dolly Porphyry	Rim on py	399	3.16	423	215	22.8	13,050	1,225	2,278	850	475
apy-6-1a-2		f-g agg	<8.53	32.7	513	218	25.7	11,046	690	2,230	2,384	364
apy-6-1a-3		sub, f-g, agg	292	71.3	387	489	25.5	6,506	740	3,314	633	70.4
apy-6-1a-4		euh, f-g, agg, in wall rock.	<47.4	116	398	566	35.6	3,410	478	644	1,386	199
apy-6-1a-5		sub, f-g, in wall rock.	<46.8	79.1	618	755	48.0	6,080	854	874	15,075	248
apy-6-1a-6		anh, porous	<59.6	177	816	724	43.1	2,594	756	3,846	2,888	243
Mean			44.9	47.8	506	438	32.1	6,078	760	1,821	2,064	229
apy-06-7a-1	WSZ	Rim on py, in wall rock	28.9	308	1,993	144	21.5	1,889	37.0	716	647	7.10
apy-06-7a-2			13.8	364	2,167	107	5.28	1,802	31.9	2,052	282	2.84
apy-06-7a-4		sub, fgd, in wall rock	<9.95	41.4	403	70.7	1.27	16,528	36.6	1,696	95.9	<0.62
apy-06-7a-5		sub, agg, in vein salvage	<5.81	13.6	280	397	4.23	3,957	27.9	5,767	106	1.95
apy-06-7a-6		In vein salvage	<4.62	85.7	671	2,047	13.1	8,037	41.4	2,180	190	2.55
apy-06-7a-7		euh, in wall rock	<6.65	869	4,071	103	13.0	2,831	22.5	398	624	5.01
SU333-3		f-g, agg	<7.8	14.0	120	120	3.01	7,182	6.06	1,797	103	1.62
SU333-4		Rim on py	<13	2.20	86	79	2.57	10,211	<11	1,874	70	19.2
SU333-5		In vein	<14	25	89	403	3.06	1,419	<12	1,433	71	1.30
SU333-6		Agg	<10	15	122	185	1.90	5,672	<7.9	1,954	74	0.95
Mean			5.75	47.1	414	191	4.64	4,442	15.7	1,611	156	2.39
SU331-1	WFZ	In vein	<26	76	295	75	<2.4	308	32	1,505	31	0.50
SU331-2			<16	65	252	37	<1.6	126	24	1,074	25	0.30
SU331-3		In wall rock	<23	27	111	<33	<2.2	220	44	131	46	0.46
SU331-4			<10	103	334	144	<1.6	340	<14.0	10.4	63	1.17
SU311-3			<5.4	3.85	86	962	10.6	88	<6.1	146	1,400	71.7
Mean			6.94	35.0	188	91.3	1.55	191	14.8	200	79.3	1.42
SU17-8	SSZ	In vein, sulfidized BIF	<18	9.84	15	29	<1.2	200	435	23.4	0.19	<0.1
Average (all arsenopyrite analyses)			16.3	53.7	459	166	5.50	1,443	135	562	182	8.65

Means are based on logarithmic value, with analyses below detection limits (DL) included at DL/2 value

euh euhedral, *sub* subhedral, *anh* anhedral, *f-g* fine-grained, *c-g* coarse-grained, *agg* aggregate, *fgd* fine-grained disseminated, *py* pyrite, *WSZ* Western Shear Zone, *WFZ* Watu Fault Zone, *SSZ* Sunrise Shear Zone
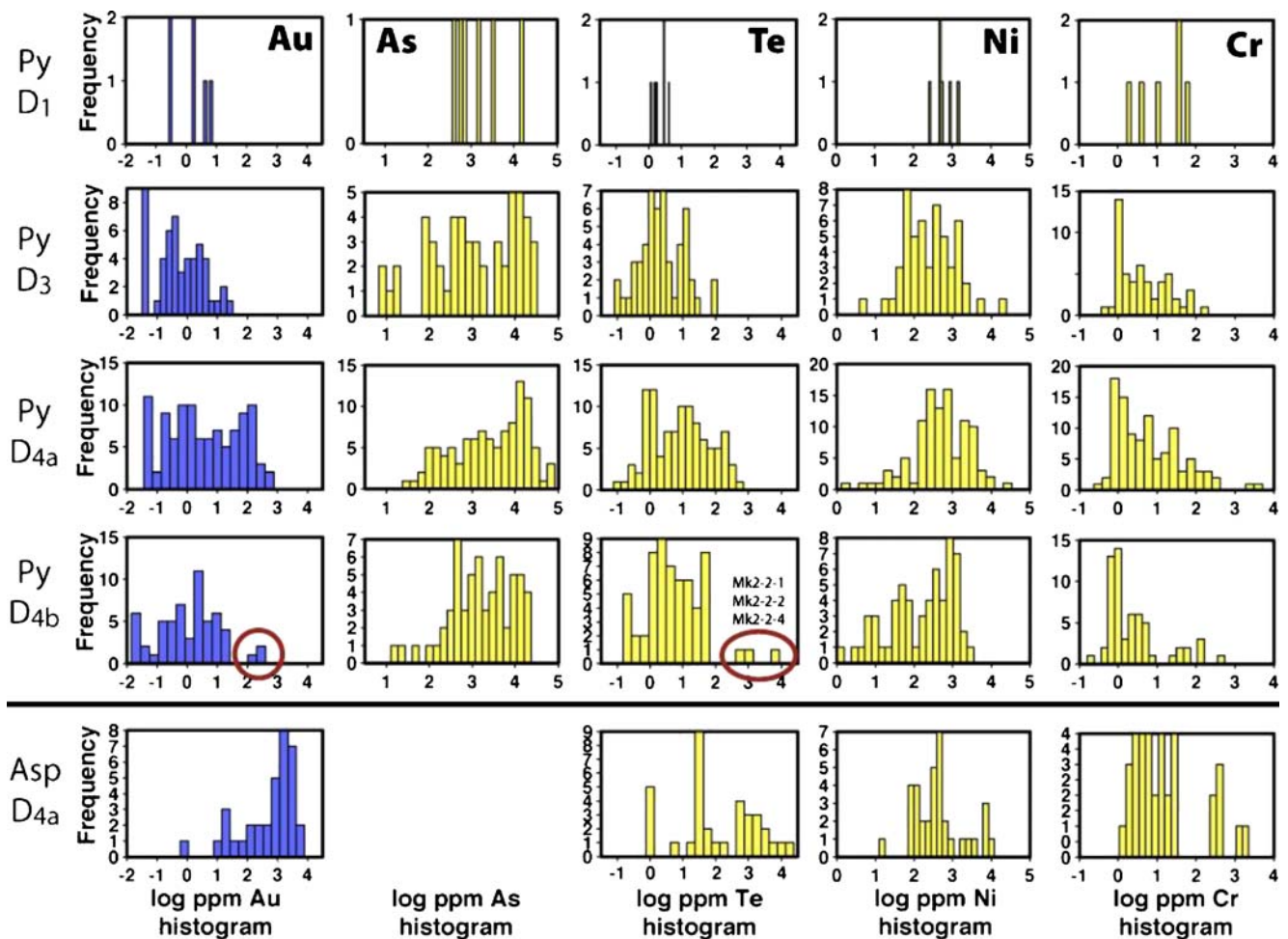
Fig. 5 Distribution of some trace elements (LA-ICP-MS data) in Sunrise Dam pyrite as a function of ore stage and arsenopyrite from the D_{4a} stage. The *circles* in Py D_{4b} (Au, Te) emphasize three analyses in sample Mk2-2 with anomalously high Au and Te concentrations
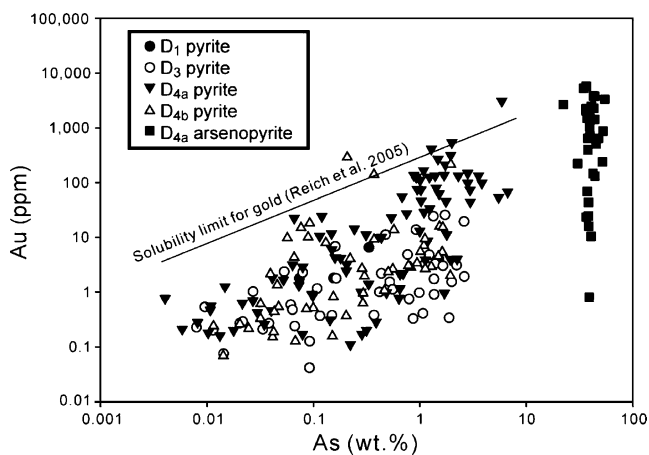

Fig. 6 Plot of Au vs. As concentrations for arsenian pyrite (as a function of ore stage) in the Sunrise Dam gold deposit analyzed by LA-ICP-MS. Solubility limit for gold is based on Reich et al. (2005). The five analyses plotting above the solubility limit were obtained on pyrite grains from the WSZ (D_{4a}) and Mako (D_{4b}) orebodies

presence of buried inclusions of Au-bearing minerals, in the case of Fig. 4e nagyágite ($Pb_5Au(Te,Sb)_4S_{5-8}$).

In contrast to pyrite, the spectra obtained for arsenopyrite are relatively similar one to another. Figure 4f shows the LA-ICP-MS profile corresponding to the highest Au concentration measured in this study. The Au signal is more erratic than that of any other element, and there is no correlation between the Au signal and that of any other element.

Textures, mineral associations, and sulfide chemistry

We investigate the trace-element contents as a function of the textures and paragenesis of the sulfide minerals. A variety of distinct pyrite and arsenopyrite textures and mineral associations occur within the Sunrise Dam orebodies, which broadly correlate with the deformation stage. Pyrites in D_{4a} and D_{4b} structures often exhibit evidence of episodic growth, recrystallization, and remobilization.
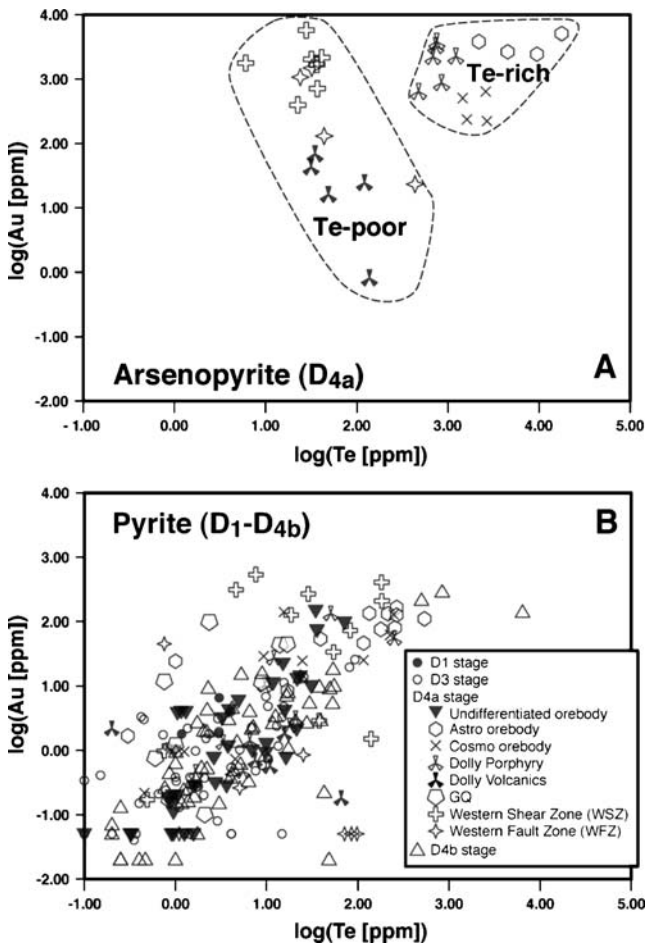
Fig. 7 Plots of Au concentrations vs. Te concentrations in arsenopy-rite (**a**) and pyrite (**b**) from the Sunrise Dam deposit, as a function of ore stage and ore deposit. Two different Au-enrichment trends are clearly visible in the arsenopyrite dataset

Pyrite from D_1 stage

D_1 pyrite occurs as fine-grained (50~120 μm), anhedral to subhedral grains associated with minor amounts of tennan-tite, chalcopyrite, and molybdenite; the sulfides are ob-served both in the vein and host rock. Gold content in the pyrite varies from less than 0.3 to 6.56 ppm Au with an average value of 1.12 ppm Au (n=6; Table 2).

Pyrite from D_3 stage

D_3 pyrite in general occurs as subhedral to anhedral grains, or as distinct pentagonal dodecahedral (pyritohedral) or cubic crystals, and commonly with sponge-like surfaces and numerous cavities. Pressure shadows often observed around coarser-grained pyrite are mainly composed of

Fig. 8 Plots of the concentrations of some trace elements in Sunrise ▶ Dam pyrite and arsenopyrite. The *symbols* for pyrite distinguish among the orebodies and ore stages. **a** Ni vs. Co; **b** Bi vs. Pb; (**c**) Ni vs. Cr
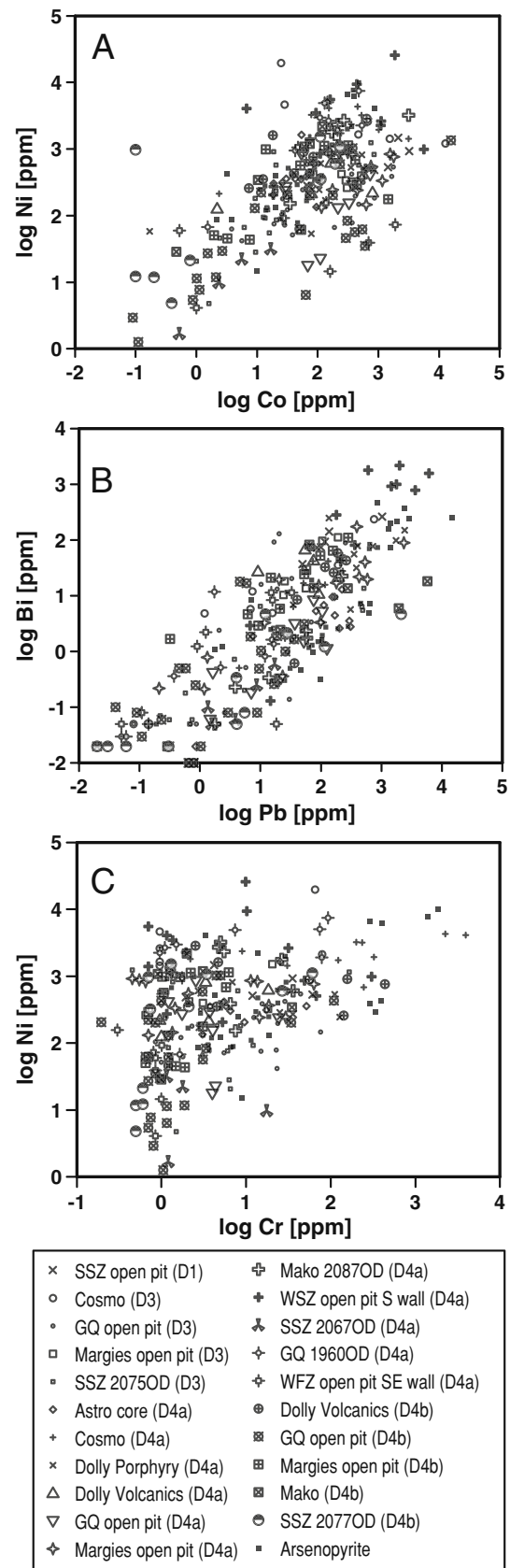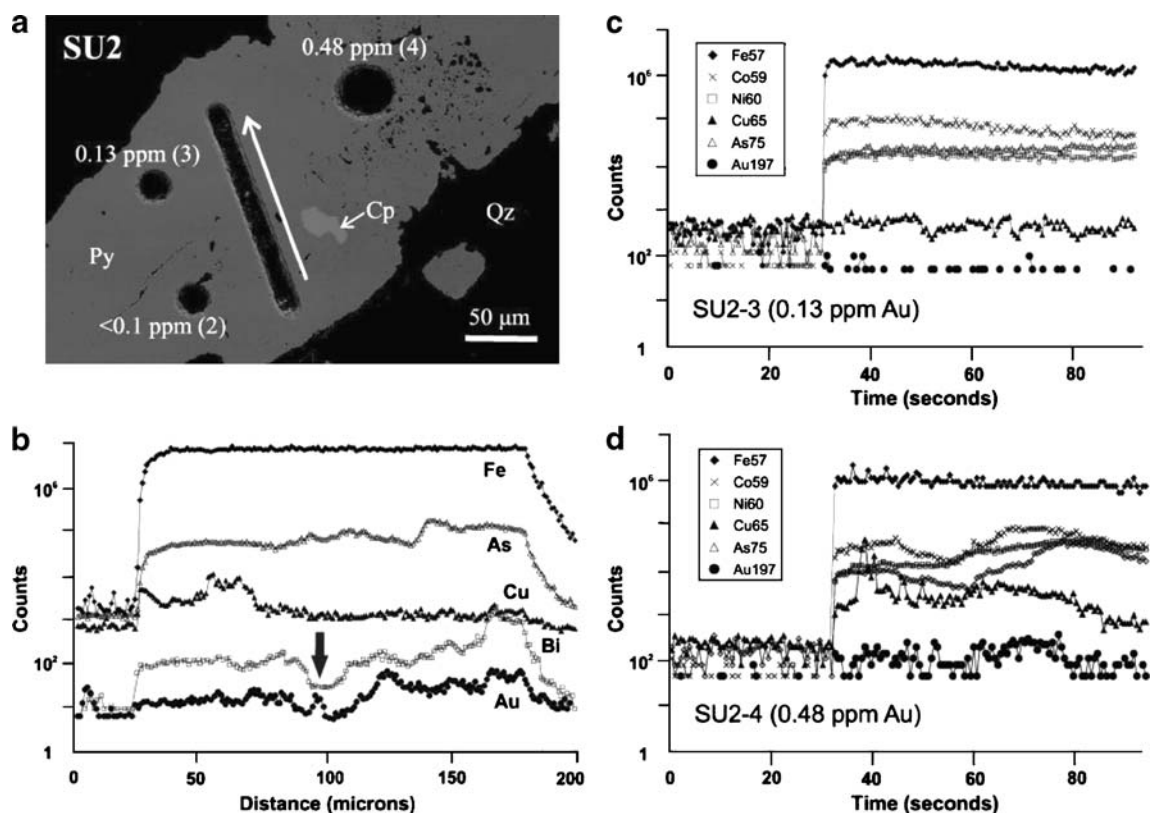
Fig. 9 Pyrite in D_3 vein. **a** Back-scattered electron image showing the location of a LA-ICP-MS line raster single and three spot analyses. Note the distribution of areas with plenty of inclusions and those with few inclusions. The *arrow* shows the direction of line raster. **b** LA-

ICP-MS line raster across the grain shown in **a**. **c**, **d** Typical ablation signals for selected elements from spots 3 and 4 in the BSE image. Abbreviations: see Table 1

elongated and curved quartz crystals. Euhedral pyrites in the BIF unit often contain a linear array of magnetite inclusions that are parallel to the orientation of magnetite banding, indicating porphyroblastic growth. The following description focuses on pyrites from three locations in the SSZ orebody, illustrating the differences between vein pyrites and those resulting from BIF sulfidation: SU2 is a small D_3 quartz vein and SU11 and SU17 illustrate increasing degrees of BIF sulfidation (Table 1).

The coarser pyrite grains in SU2 contain locally abundant minute inclusions of gangue minerals (Fig. 9a). Although such grains appear otherwise homogeneous under the SEM, a qualitative LA-ICP-MS profile across a grain shows significant variations in the Au and As signals, with an As- and Au-poor "zone" followed by an As- and Au-rich portion (Fig. 9b). The Au concentrations also appear to be positively correlated with Bi concentrations. Three spot analyses (Appendix) confirm this internal inhomogeneity: Au concentrations vary from <0.15 (in the inclusion-poor areas) to 0.48 ppm (inclusions-rich area). There are also some marked differences in the time-resolved depth profiles in LA-ICP-MS analyses (Fig. 9c, d). Co and Ni in spot 3 are detected as relatively steady lines over the

time-integrated ablation (Fig. 9c), but significant variations with depth are observed from the spots 2 and 4 (e.g., Fig. 9d) suggesting compositional zoning with depth within the pyrite crystal. A spiky pattern in the Cu signal clearly indicates the presence of buried chalcopyrite inclusions; a larger (50 μm) chalcopyrite inclusion is visible in Fig. 9a.

Sample SU11 is a near-pristine BIF containing only minor amounts of pyrite, occurring as subhedral to anhedral fine (<100 μm) grains scattered in magnetite–quartz–dolomite–ankerite bands. Ankerite or ferroan dolomite is observed as infill between grain boundaries of subhedral magnetite. In addition, scheelite and chalcopyrite are found in trace amounts. One spot analysis shows 0.38 ppm Au. In contrast, in the highly sulfidized BIF sample SU17, pyrite is the dominant ore mineral, having replaced most of the original magnetite. This pyrite is coarser-grained and more porous than that in less sulfidized BIF. Fine-grained magnetite is disseminated sparsely and euhedral arsenopyrite crystals are found along selvages of the ankerite veins. Larger pyrite crystals in SU17 display very characteristic microstructures, which are interpreted as overgrowth of D_3 pyrite during D_{4a} (see below; Fig. 10e).

Fig. 10 Back-scattered electron images of textures of pyrite from the D4 stage at the Sunrise Dam deposit. **a** D_{4a} stage pyrite crystal enclosed by galena, tennantite, and chalcopyrite from WFZ, showing patchy As zoning. **b** Pyrite with three distinct growth zones marked as *I*, *II*, and *III*, from a quartz vein in the Cosmo orebody. **c** Pyrite with the same three distinct growth zones as in **b**, but from a highly sulfidized BIF. The *white square* indicates the location of a detail shown in **d**. **d** Detail of zone II of the pyrite crystal shown in **c**, showing crystallographically oriented arsenopyrite (*white*) and gangue minerals (*dark spots*). **e** D_3 (?) idiomorphic pyrite crystal showing a reaction-front rich in As; pyrite behind the reaction front displays porosity and many small gangue inclusions. **f** Small (40-μm) pyrite crystal recovered from the tailings dam, showing an As-rich core partially replaced by As-poor pyrite with numerous inclusions of arsenopyrite and increased porosity (filled with quartz). **g**, **h** D_{4b} stage pyrite, showing inclusions of native gold, chalcopyrite, sphalerite, and tennantite (**g**) and association with telluride (**h**). Abbreviations: see Table 1
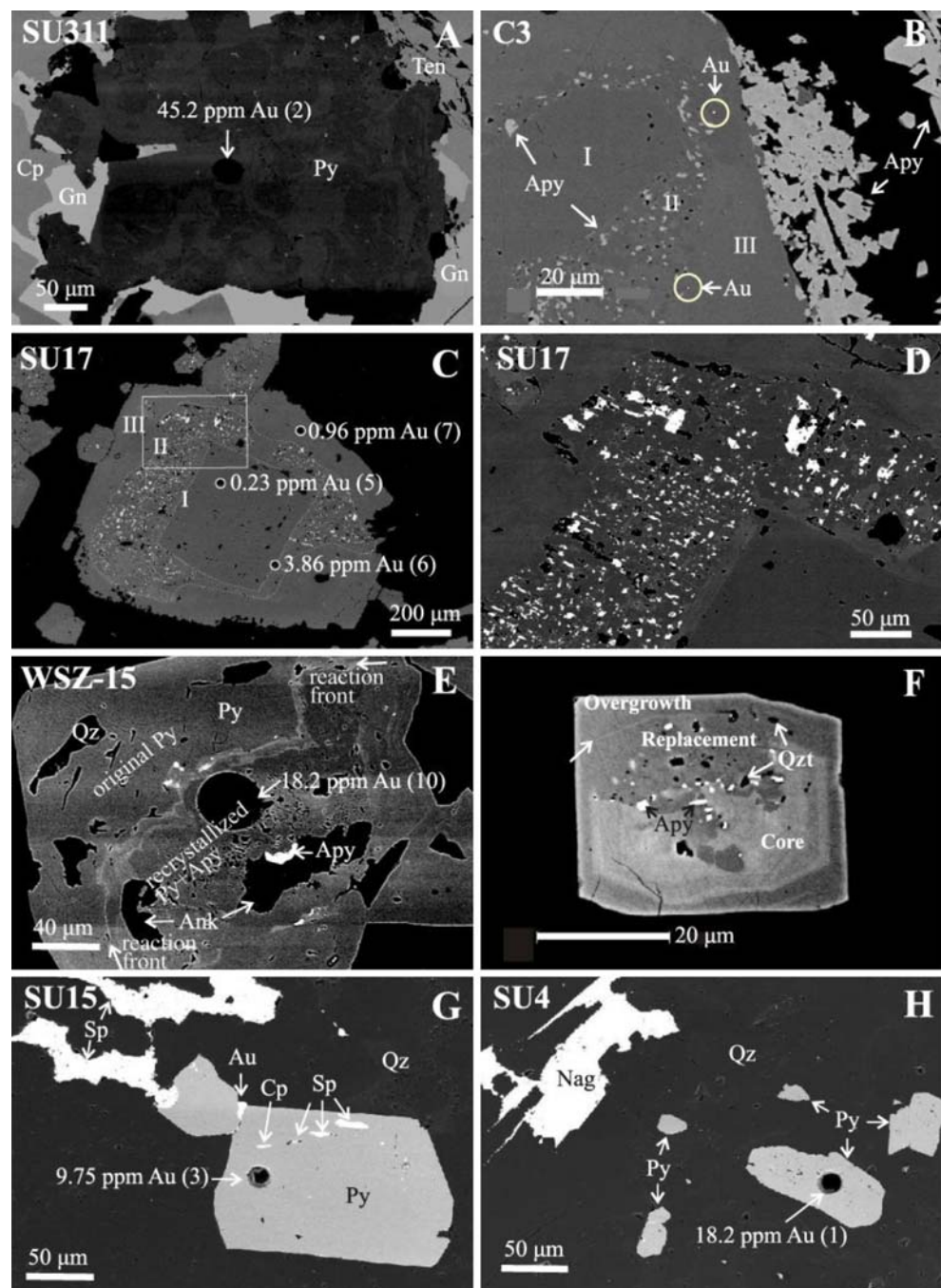
Pyrite and arsenopyrite from D_{4a} stage

D_{4a} pyrite crystals were identified in all the studied orebodies (see Table 1). Pyrite from D_{4a} veins commonly occurs as subhedral to anhedral grains with numerous pores or inclusions of silicates, carbonates, oxides, sulfides, and minor telluride minerals.

In the WSZ, most pyrite consists of agglomerates of euhedral to subhedral crystals that are overgrown or completely rimmed by euhedral arsenopyrite. EMP results show that these pyrites have distinctively higher arsenic content (average 1.27 wt.%) than those from other stages or orebodies in the deposit, though the As distribution in these pyrites is somewhat patchy (evidence of episodic growth or recrystallization). Pyrite in the WSZ is disseminated within altered intermediate volcanic rocks and infrequently replaced by arsenopyrite near ankerite veins.

Some pyrite from the GQ orebody contains inclusions of chromite (abundant), melonite ($NiTe_2$), and gersdorffite. Other associated minor inclusions include altaite (PbTe), quartz, K-feldspar, rutile, titanite, sericite, monazite, dolomite, ankerite, and tourmaline. The Cr concentrations

obtained from these pyrites can exceed 100 ppm (Fig. 8c); similar high (and higher) concentrations are found in D_{4a} pyrite from the nearby Cosmo orebody. These high Cr contents generally also are coupled with high Ni and Co contents (Fig. 8a). Overgrowth textures are very common in the D_{4a} pyrite from GQ and native gold is found as inclusions in pyrite or fills the fractures of pyrite either as separate grains or intergrown with gersdorffite. Au and Te concentrations in GQ pyrite are variable, from below detection limits to 22.4 ppm Au and 21.3 ppm Te. The overgrown pyrite contains lower Au concentration (Table 4 in Appendix) and there is generally a positive correlation between As and Au concentrations.

In the WFZ orebody, the arsenian pyrite (1.76 wt.% As) is sometimes enclosed successively by galena, tennantite, and chalcopyrite. BSE images reveal that the pyrite is composed of numerous irregular domains within an As-richer groundmass (Fig. 10a). Tetradymite (Bi_2Te_2S) was found as rare inclusions in pyrite from the WFZ orebody, either enclosed in pyrite, or sealing fractures in pyrite together with native gold. A single analysis of a pyrite with inclusions of tetradymite and native gold showed 0.85 ppm Au, 25.3 ppm Te, and 11.4 ppm Bi.

Many D_{4a} pyrites display a characteristic zoning consisting of three distinct zones (Fig. 10b, c): (I) a porous core of lowest As content surrounded by a narrow As-richer zone, (II) a porous inclusion-rich (mainly arsenopyrite with minor galena, quartz, feldspar, Mg–Fe carbonates; e.g., Fig. 10d) zone displaying corona-like texture, and (III) an outermost overgrowth zone consisting of bands or layers with different As contents. A change in the crystal morphology during the growth of these crystals is also noticeable; the cores through to zone II show cube or octahedral forms, subsequently changing to pyritohedron whose orientations are at a slight angle to the outline of the cores, indicating deformation during crystal growth. Coarse-grained pyrites often have corroded margins indicating dissolution. Such zoning is common among coarse crystals in sulfidized BIF from WSZ (Fig. 10c) and in As-rich quartz veins from the Cosmo orebody (Fig. 10b). There are wide variations in Au contents within the three different zones. The highest Au concentrations of up to 148.7 ppm were found in zone II (spot SU17-2), whereas the core (zone I) in the same grain has the lowest Au content (0.38 ppm, spot SU17-1). The LA-ICP-MS Au-profile indicates the presence of native gold inclusions near the surface, and this interpretation is supported by the occurrence of tiny native gold grains (<400 nm) in zone II of multiply overgrown pyrites from the Astro orebody. Similar evidence exists for the presence of micro-inclusions of a Pb–Sb sulfide or sulfosalt in zone II of these pyrites. The core (zone I) regions of these zoned pyrites are quite similar to those from less sulfidized BIF and may represent D_3 pyrite.

Another style of complex zoning in arsenian pyrite is characterized by textures suggestive of recrystallization along a reaction front (Fig. 10e, f). The reaction front in the crystal shown in Fig. 10e is underlined by As-rich composition; the pyrite behind the front has higher porosity than the "pristine" pyrite. The crystal shown in Fig. 10f has been retrieved from the tailing dams, but was left untouched by the processing. It has an As-rich core with weak oscillatory zoning and an overgrowth of As-poor pyrite. A large part of the core has been replaced by As-poor pyrite, with a composition similar to the overgrowth. This replaced pyrite is characterized by many inclusions of arsenopyrite as well as pores and shows a sharp and convolute contact with the core. The arrow on Fig. 10f points to an As-rich "ghost" that still underlines the original limit between the original crystal and an overgrowth with the same composition as the replacement.

Arsenopyrite occurs generally as idiomorphic, lath-, or rhomb-shaped crystals ranging in size between 50 and 200 μm in diameter, but occasionally reaching several mm in the Dolly Volcanic. Single crystals are dispersed in the host rocks or are concentrated in aggregates of numerous intergrown individuals occurring in thin interlayers and selvages of the ankerite veins and wall rock fragments in the veins. The arsenopyrite crystals generally show preferred orientation parallel to the schistosity of host lithologies. In some cases, rosettes of euhedral arsenopyrite crystals rim pyrite (e.g., Fig. 10b) and fine-grained euhedral arsenopyrite occurs as inclusions within pyrite crystals. When observed by BSE imaging, most arsenopyrite crystals display compositional zoning related to the As contents. Electron microprobe analyses reveal that arsenopyrite is systematically As deficient, ranging from 25.7 to 30.4 at.% As (33 at.% is the stoichiometric value). Such As deficiency is common in Archaean orogenic Au deposits, and these values place Sunrise Dam among the "Au-bearing arsenical type" deposits in the classification of Vaughan and Kyin (2004). Arsenopyrite from the Astro orebody has the lowest average As (26.22 at.%), whereas the highest average As content (30.23 at.%) is found in coarse-grained arsenopyrite in the Dolly Volcanic orebody. The As zoning in arsenopyrite seems to be more complex in the ore veins compared to that in the wall rock. Rims of arsenopyrite crystals are usually richer in As than the cores (Fig. 11a), most likely from a change in fluid composition or temperature during crystallization. The crystal in Fig. 11b displays a different type of As zoning: The complex patchy zoning is related to crystallographic control of composition, most probably through polysynthetic twinning.

In most cases, arsenopyrite in veins or vein salvages shows Au concentrations that are one to two orders of magnitude higher than in wall rock arsenopyrite (Table 3). A euhedral arsenopyrite crystal from highly sulfidized BIF

Fig. 11 SEM back-scattered electron images of arsenopyrite textures from the WSZ at the Sunrise Dam deposit; brighter areas contain more arsenic. **a** Zoning in fine-grained arsenopyrite. Sample WSZ333. **b** Twinned arsenopyrite crystal with inhomogeneous As content. Sample SU7. Abbreviations as in Table 1
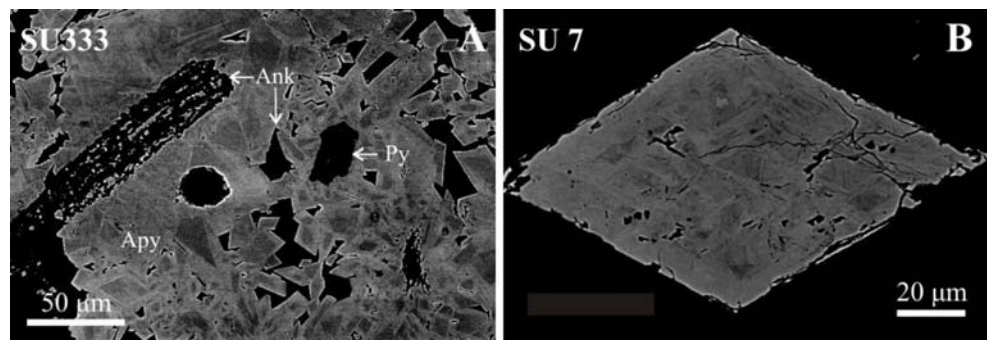
also contains 23.4 ppm Au and elevated Te concentrations up to 435 ppm (spot SU17-8). The highest Au value was measured in a sample from the Astro orebody (Table 3). Although this value is anomalously high, the ablated Te signals exhibit smooth profiles and a good correlation with As and Fe signals. Thus, Te appears to be present in solid solution in the crystal structure of arsenopyrite.

D_{4b} stage

D_{4b} vein pyrites occur mostly as subhedral to euhedral grains (20 μm to ~2 mm in size; type 1_{eh}) and aggregates (type 1_{ag}) possessing a pyritohedral or cubic form. Locally, smaller (0.1–10 μm) euhedral to subhedral disseminated grains are also present (type 2). In some parts of D_{4b} quartz veins that show swelling, subhedral to anhedral pyrite (type 1_{sw}) is accompanied by other sulfides (sphalerite, galena), sulfosalts (tetrahedrite, bournonite), and nagyágite (Fig. 10h). Rare skeletal pyrite grains (type 3) are found in quartz veins that also contain pyrite grains (up to 1 mm in length) with inclusions of native gold. In contrast to other pyrite from Sunrise Dam, many D_{4b} pyrite crystals contain micrometer-sized native gold inclusions (e.g., Fig. 10g). Other minerals found as inclusions in D_{4b} pyrite include hessite, chalcopyrite, tennantite, galena, cassiterite, quartz, K-feldspar, fluorapatite, monazite, xenotime, ankerite, and dolomite. Among these, the sulfides and sulfosalts are generally aligned parallel to the growth planes, indicating pre- or *syn*-tectonic growth of D_{4b} pyrite, under relatively stable conditions allowing the nucleation of ore minerals on the pyrite surface. In contrast, silicate and carbonate inclusions generally occur as mineral aggregates with semi-oriented texture at the margin, providing evidence for fluid pressure fluctuations during pyrite growth (Ciobanu et al. 2004).

Concentrations of 0.52 to 18.2 ppm Au, 2.22 to 53.3 ppm Te, and 922 to 5,053 ppm As were obtained from type 1_{sw} pyrite grains (spot SU4-1, SU4-2, and SU10-2; Table 4 in Appendix). Laser ablation profiles show that gold has positive correlations with Te, Pb, Sb, and Ag rather than with As (e.g., Fig. 4e), indicating that Au is present mainly in the form of nagyágite inclusions.

Silver content of native gold

Coarse native gold is found within the different mineralizing stages and alteration zones throughout the deposit, but D_{4b} veins are characterized by a large number of particulate gold grains, mainly occurring as inclusions within pyrite or along microfractures and grain boundaries in pyrite (e.g., Fig. 10g). They also occur in tetrahedrite–tennantite, galena, sphalerite, nagyágite, altaite, and Au–(Ag)–As–telluride and are intergrown with hessite and tetradymite.

EMP analyses revealed that gold is alloyed with silver at Sunrise Dam, with Ag concentrations ranging from 2.78 to 42.80 wt.%. The purest gold (97.2 wt.% Au; $n=6$) occurs as coarse free gold in ankerite veins from the D_{4a} stage. Native gold in intermediate volcanic rocks from WSZ (D_3 or D_{4a} stage) is also relatively pure (average 96.4 wt.%, $n=6$), as is native gold from the decomposition of nagyágite (average 94.6 wt.%, $n=7$). Native gold in D_{4b} structures shows a wide variability: gold inclusions in D_{4b} pyrite have an average Au content of 91.8 wt.% ($n=12$), free gold in D_{4b} quartz vein 84.7 wt.% ($n=5$), and the lowest purity (56.9 wt.% Au) was found in electrum filling fractures in D_{4b} pyrite.

Discussion

Gold incorporation in sulfides

In natural arsenian pyrite, the highest reported Au concentration exceeds 1.1 wt.% (Pals and Spry 2003; Pals et al. 2003), but a maximum Au content of only 0.64 wt.% was obtained from synthetic arsenian pyrite (Fleet and Mumin 1997). In contrast, gold values up to 1.52 wt.% have been reported in natural arsenopyrite (Johan et al. 1989), and Fleet and Mumin (1997) prepared synthetic arsenopyrite containing up to 3.0 wt.% Au. Vaughan and Kyin (2004) used secondary ion mass spectrometry measurements on arsenian pyrite and arsenopyrite to characterize refractory Au ores from nine mesothermal Au deposits in the Yilgarn Craton. They reported maximum Au contents of 327 ppm (average 43 ppm) for arsenian pyrite from Wiluna (Norseman-Wiluna Belt, ~345 km NW of Sunrise Dam)

and 1,069 ppm (average 276 ppm) for arsenopyrite from Lancefield (Laverton Greenstone Belt, ~65 km N of Sunrise Dam). Highly refractory arsenical ores are predominant in both of these deposits.

The LA-ICP-MS data in this study indicate that arsenian pyrite and arsenopyrite in the Sunrise Dam deposit incorporate significant amounts of refractory Au. The average Au content in arsenian pyrite is 1.61 ppm ($n=224$) with a maximum value of 3,067 ppm from the WSZ orebody. In arsenopyrite, the average Au content is 562 ppm ($n=35$), with a maximum value of 5,767 ppm. The highest Au values, both average and maximum, are obtained from D_{4a} stage pyrite and arsenopyrite, which is consistent with D_4 being the major mineralizing event in the deposit. The average Au concentration (calculated using raw parts per million values) in arsenian pyrite is almost 20 times higher than that from Lancefield (21.0 vs. 1.2 ppm Au), but is lower than that from the Wiluna deposit (43 ppm Au). The Au concentrations in the Sunrise Dam arsenopyrite are the highest yet reported in the Yilgarn Craton and are even higher than those reported from the arsenopyrite-rich Ashanti mesothermal deposit in the Ashanti Belt of Ghana (1 to 2,500 ppm, average 190 ppm Au; Oberthür et al. 1997). Our data indicate a preferred enrichment of Au in arsenopyrite relative to coexisting pyrite (e.g., Fig. 5); such preferential enrichment has not only been documented in the Yilgarn (e.g., Vaughan and Kyin 2004; Morey et al. 2008) but also from many gold deposits worldwide (e.g., Mumin et al. 1994; Fleet and Mumin 1997).

Element correlations and the nature of LA-ICP-MS traces indicate that Au occurs in different forms in sulfides from Sunrise Dam, including "invisible gold" (either solid solution in the crystal lattice or nanoparticles <100 nm in size), particulate native gold, and Au compounds, notably tellurides. The complexity of the paragenesis and speciation of Au found at Sunrise Dam is the result of a number of different processes, active at different scales. The most likely contributors are:

1. *Different mechanisms for mineral precipitation.* Brown et al. (2003) suggests that two main processes resulted in Au deposition at Sunrise Dam: desulfidation of the hydrothermal fluid caused by fluid–rock interaction, resulting in the destabilization of the Au(I)–bisulfide complexes in solution (D_3–D_{4a}), and phase separation during D_{4b}. At Sunrise Dam, two types of lithologies are particularly rich in Fe(II) and hence highly reactive in the presence of a bisulfide-bearing hydrothermal fluid: BIF and (ultra-) mafic rocks. Both lithologies appear to have reacted with D_3/D_{4a} hydrothermal fluids, causing significant Au mineralization. Intermediate volcanic and volcanoclastic rocks also can participate in scavenging sulfur from the hydrothermal fluid.

2. *Different mechanisms for Au incorporation in sulfides.* The role of As-rich sulfides, foremost arsenian pyrite and arsenopyrite, in scavenging Au has been long recognized, but the scavenging mechanism remains controversial. Several mechanisms have been proposed that may all be active under specific conditions. These mechanisms range from surface electrochemical reactions (e.g., Maddox et al. 1998), to chemisorption (e.g., Fleet and Mumin 1997), and to highly reducing conditions localized at the surface of arsenic-rich minerals during dissolution (Pokrovski et al. 2002).

3. *Local redistribution of Au*—and possibly upgrading of Au grades—during remobilization of preexisting Au mineralization. This aspect may have been underestimated in many polyphase Au deposits, and we will demonstrate how dissolution–reprecipitation reactions may account for a significant upgrading of Au grades at Sunrise Dam.

In the next section, we attempt to identify some of the factors that result in the complex Au speciation observed at Sunrise Dam.

Sulfidation reactions: BIF vs. (ultra-) mafic vs. intermediate volcanic and volcanoclastic rocks

Pyrite from partially sulfidized BIF and core zones of pyrite (zone I) in highly sulfidized BIF contain low Au concentrations (<0.4 ppm) and relatively low concentrations of trace elements (Table 4 in Appendix). These pyrite crystals likely grew during D_3. The low Au concentrations may reflect sulfidation from a Au-poor fluid, or the inefficiency of the sulfidation reaction in affecting Au solubility under the conditions of formation of this pyrite. The higher Au concentrations in zones II and III could indicate that Au solubility was controlled by the activity of bisulfide in the fluid, itself controlled by the extent of fluid–rock interaction (amount of pyrite formed); however, the texture suggests that zone II resulted from the recrystallization of a preexisting pyrite during D_{4a} (see below) and hence that the higher Au concentrations are more likely related to a different Au-scavenging process or to different physical and chemical conditions.

The GQ orebody at the 1960 ore drive is mainly composed of arsenian pyrite with minor amounts of Cr–Ni–Ti minerals and tellurides. The As and Au contents are higher in the core of these pyrites than in the overgrowth, implying that deposition of pyrite was initiated from Au–As–(Te)-rich fluids followed by progressive overgrowth of pyrite from more dilute fluid, possibly during the waning stage of D_{4a} mineralization. The nature of the host rock protolith is hidden by a very strong carbonate–sericite alteration, but the Cr contents of the sericite ("fuchsite") and the chemistry of the GQ pyrite provide very strong evidence that the altered

host rock had some (ultra-) mafic affiliation. It displays elevated contents of Cr (up to 92.9 ppm), Co (up to 537 ppm), and Ni (up to 7,474 ppm). Moreover, GQ pyrite preserves inclusions of relict chromite, which most likely represents the source of Cr found in the secondary "fuchsite". The presence of Ni-bearing minerals (e.g., gersdorffite), which is restricted to Cr-rich assemblages, also is consistent with the (ultra-) mafic nature of the protolith.

A similar situation exists in the Cosmo orebody at the 1940 ore drive, where both pyrite (D_3 and D_{4a}) and arsenopyrite (D_{4a}) are enriched in Cr, Co, and Ni (Tables 2 and 3). Coarser pyrite grains in D_3 stage contain inclusions of pyrrhotite, indicating a reducing character and/or higher temperature environment (Mernagh et al. 2004). In contrast to the GQ orebody, Cr- or Ni-bearing minerals were not observed at Cosmo; however, elevated contents of Cr, Ni, and Co in sulfide minerals may reflect an affiliation with (ultra-) mafic host rocks.

In a location where the WFZ orebody is hosted in intermediate volcanic rock, high Au (45.2 ppm) and As (1.76 wt.%) concentrations occur in pyrite successively encapsulated by other sulfide and sulfosalt minerals (Fig. 10b). Textural evidence and high As contents suggest that the pyrite was precipitated from D_{4a} stage ore fluids enriched in As and Au and that it retained its original chemical composition during later mineralizing events. Judging from the smooth and flat profile of the laser ablation signal (Fig. 9b), Au is likely to occur in a chemically bonded form. Pyrite containing inclusions of tetradymite and native gold shows elevated contents of Bi and strong correlation with the Au signal. This association is interpreted as a geochemical affinity between Au and Bi and their simultaneous incorporation into pyrite structure from the D_{4a} mineralizing fluid that formed tetradymite and native gold. Moreover, differences in chemistry and inclusion mineralogy in D_{4a} pyrites from GQ and WFZ are also interpreted to reflect the influence of local fluid–rock interaction; it is possible that the Bi was derived locally from the intermediate volcanic rocks.

The above examples confirm that fluid–rock interaction was a major precipitation mechanism for sulfides in D_3/D_{4a} stages. In many cases, the nature of the host rock affected the chemistry of pyrite. It is also noticeable that the early BIF sulfidation reactions did not produce high Au grades at Sunrise Dam, most probably reflecting strong undersaturation of the mineralizing fluids with respect to gold during the sulfidation.

Association of Au–As and Au–Te–(Sb)

Refractory Au is commonly incorporated within the structures of arsenian pyrite and arsenopyrite, and it has a strong affinity to As content of arsenian pyrite and inversely correlates with

the Fe content of arsenopyrite (e.g., Wu and Deldove 1989; Cook and Chryssoulis 1990; Fleet et al. 1993; Yang et al. 1998; Pals et al. 2003). LA-ICP-MS analyses of arsenian pyrite from the Sunrise Dam deposit show a positive correlation between Au and As (Fig. 6), which is common for invisible gold-bearing arsenian pyrites elsewhere (e.g., Arehart et al. 1993; Cook and Chryssoulis 1990; Ashley et al. 2000; Pals et al. 2003). Furthermore, Au contents in pyrite also have a positive correlation with Te (Fig. 7b). In contrast, a plot of Au and Te values from arsenopyrite (Fig. 7a) distinguishes two arsenopyrite populations. Arsenopyrite from the Astro, Cosmo, and Dolly Porphyry orebodies are relatively Te rich and show a weak positive correlation between the Au and Te concentrations. Arsenopyrite from the other orebodies has lower Te concentrations and no, or a slightly negative, correlation between Te and Au. The Astro, Cosmo, and Dolly Porphyry orebodies are within and adjacent to porphyry intrusions, and the As–Te–Au signature may reflect this lithological association.

Gold concentrations in arsenopyrite are inversely correlated with grain size: Arsenopyrite crystals in the Dolly Volcanic are coarse-grained (up to several millimeters in length) with lower average Au values (15.7 ppm Au, $N=5$), whereas finer grained (<100 μm) arsenopyrite crystals in the WSZ have much higher average Au concentrations of 1,611 ppm ($N=10$); this relationship is consistent with the findings of Vaughan and Kyin (2004) in that finer-grained arsenopyrite from gold deposits in the Yilgarn Craton generally contains higher concentrations of refractory gold. It is noteworthy that pyrite and arsenopyrite in porphyry host rock, even within a single orebody such as Dolly, have higher average Au concentrations (4.79 ppm in pyrite and 1,821 ppm in arsenopyrite) than those from volcanic host rock (0.78 ppm in pyrite and 15.7 ppm in arsenopyrite). Because volcanic rocks are less competent than porphyry (Brown et al. 2002), they are inferred to have hosted coarser-grained (but comparatively Au-depleted) sulfide minerals by providing a suitable porosity compared with adjacent rhyodacite porphyry.

According to Reich et al. (2005), the solubility of gold in arsenian pyrite from Carlin-type and epithermal Au deposits increases with the amount of As. They argued that high Au values above the solubility limit correspond to particulate native gold (Au^0), whereas those below the limit represent structurally bound Au occurring as solid solution (Au^+). At Sunrise Dam, five data points plot above or on the Au solubility line (Fig. 6), three of them are from WSZ (D_{4a}) and two from Mako (D_{4b}). The presence of metallic gold in the sampled volume is suggested by the spiky pattern of ablated signals, and, in some cases, SEM imaging revealed the presence of submicrometer-sized native gold particles. All the other analyses fall below the Au solubility limit. However, metallic Au inclusions still exist below the Au solubility limit

in some pyrites grains from sulfidized BIF, D_{4b} pyrite, and D_3 (Fig. 4a). This discrepancy may result from different formation mechanisms and/or environment between Carlin-type and Archean orogenic Au deposits. The former type is lower temperature (150~250°C) and contains Au that is incorporated during the growth of As-rich bands in arsenian pyrite (Fleet et al. 1993). The presence of particulate gold below the Au solubility limit in the Sunrise Dam pyrite is interpreted as an evidence of the migration (remobilization) of submicroscopic gold from the arsenian pyrite lattice into inclusions during dissolution–reprecipitation (D_{4a}) and recrystallization (post-D_{4b}) process (see below).

As reported by Genkin et al. (1998) and Vaughan and Kyin (2004), Au-bearing arsenopyrite in mesothermal deposits is usually As deficient (27–32 at.%), with the most As-deficient varieties usually carrying the highest Au contents. Vaughan and Kyin (2005) found that arsenopyrite in highly refractory ores in the Yilgarn Craton contains high average concentrations (based on raw values) of invisible Au ranging from 60 to 270 ppm without any native gold inclusions (>100 nm). For example, arsenopyrite from the Lancefield deposit is As deficient (28.2–32.0 at.%), fine grained (average 20 μm), and occurs within a shear zone that crosscuts earlier formed pyrite and pyrrhotite (Vaughan and Kyin 2004). For Sunrise Dam, the occurrence of arsenopyrite is similar to Lancefield, in that arsenopyrite replaces pyrite near the vein salvages, but the arsenic content is much lower (25.7–30.4 at.%) and the concentration of invisible Au is much higher, ranging from 0.8 to 5,767 ppm with an average of 562 ppm (log based) compared to 0.1 to 1,069 ppm with an average 276 ppm at Lancefield.

D_{4b} stage mineralization is characterized by the relative abundance of Sb–Te–Pb–Zn minerals and by a varied assemblage of telluride minerals. D_4 stage mineralization began with steeper veins (D_{4a}) and concluded in the formation of gently dipping veins (D_{4b}) by pressure failure or change of stress field. Based on such an assumption, it is suggested that nagyágite was formed from residual remobilizates, which were enriched in base metals, Sb, and Au, whereas the later replacement of these minerals resulted from destabilization by fluids generated during a post-D_{4b} event (Sung et al. 2007). The pyrite associated with nagyágite shows Au concentrations as high as 18.2 ppm and has a positive correlation with Te, Pb, Sb, and Ag (Figs. 6 and 8); this is related to the presence of small inclusions of nagyágite and probably reflects the geochemical signature of the D_{4b} stage. This suggests coeval precipitation of pyrite and nagyágite.

Hence, invisible gold in Sunrise Dam pyrite and arsenopyrite is correlated to the As and/or Te contents in these minerals. Whereas arsenopyrite appears to contain mainly "invisible" gold, pyrite from different stages and different localities within a single stage show either invisible gold, native gold inclusions, or telluride inclu-

sions. On the one side, this not only reflects the greater susceptibility of arsenian pyrite to recrystallization and gold remobilization but also a wider range of conditions for pyrite crystallization. In particular, the relatively As-poor and Te-rich D_{4b} stage is characterized by coprecipitation of gold with pyrite as Au–telluride inclusions, as well as remobilization of invisible gold to native gold inclusions.

Remobilization of invisible Au

Sung et al. (2007) described the breakdown of nagyágite to native gold, altaite, galena, aurostibite ($AuSb_2$), and semseyite ($Pb_9Sb_8S_{21}$), as a result of tectonic activity that took place late to post-D_{4b}. This illustrates how postdepositional processes can affect the speciation of gold. It is likely that similar processes affected D_{4b} stage pyrite.

In contrast to those formed during the D_1, D_3, and D_{4a} stages, the coarser pyrite grains in the D_{4b} stage generally contain numerous native gold inclusions, and Au concentrations are not correlated with the As contents, e.g., As-rich rims do not contain any detectable Au (spot SU5-3 in Appendix), whereas the relatively As-poor core tends to have higher Au contents (10.1 ppm, spot SU5-2). In the latter case, the Au content appears to coincide with elevated Te, Ag, and Pb values (Fig. 4e), probably due to small inclusions of telluride minerals incorporated during the early stage of pyrite crystallization. These features can be explained by assuming that recrystallization during a late to post-D_{4b} event has caused an increase in grain size, resulting in the liberation of structurally bound Au from the pyrite lattice (Larocque et al. 1995; McClenaghan et al. 2004; Vaughan and Kyin 2004). Remobilized Au may (1) be precipitated as native gold inclusions, which are oriented parallel to the crystal face; (2) infill fractures as native gold, together with other ore minerals including chalcopyrite, galena, tennantite, and hessite (e.g., Fig. 10g); or (3) be redeposited as invisible Au, as illustrated by Au concentrations up to 15 ppm in small pyrite grains, which crystallized later than adjacent coarser-grained pyrite (spots SU15-3 and SU15-4; Appendix). The majority of native gold grains (ca. 60%) in the D_{4b} stage are found within, or in contact with, sulfides, sulfosalts, and tellurides rather than in quartz vein (12%). This implies that Au remobilized from D_{4b} pyrite reprecipitated more or less in situ, within the same sulfur- and telluride-rich environment, probably restricted to centimeter-scale migrations. The appearance of visible gold as a result of arsenian pyrite recrystallization is a common feature in Au deposits (e.g., Coleman 1957; Mumin et al. 1994; Genkin et al. 1998) and has been recently described in six deposits from the Eastern Goldfields of the Yilgarn Craton (Morey et al. 2008).

Preferential enrichment of Au in arsenopyrite seems to reflect primary coprecipitation and not the result of postdeposition processes. The lack of remobilization of the

arsenopyrite-hosted Au is supported by the fact that there is no native gold occurring either as fracture fill or overgrowths on the auriferous arsenopyrite. Particulate gold grains are rare in arsenopyrite (e.g., Mumin et al. 1994), and according to the BSE images, the rim of arsenopyrite still tends to be As richer (Fig. 11a). Therefore, in sharp contrast with pyrite, post-D_{4a} Au remobilization and redistribution does not appear to have affected the Au contents and Au speciation in arsenopyrite at the Sunrise Dam deposit.

Arsenopyrite is more refractory than pyrite and commonly retains higher levels of invisible Au (Vaughan and Kyin 2004). However, there is evidence that arsenopyrite easily re-equilibrates during peak metamorphism, resulting in the liberation of Au (Mumin et al. 1994) and As from the outer rim (e.g., Larocque et al. 1995; Lentz 2002). Therefore, preservation of compositional zoning and non-uniform compositions within individual arsenopyrite grains in the Sunrise Dam (Fig. 11a, b) are most consistent with *syn-* to postpeak metamorphism mineralization (Neumayr et al. 1993; Tarnocai et al. 1997).

The role of coupled dissolution–reprecipitation reactions in upgrading Au grades

As demonstrated above, recrystallization reactions are important in controlling Au speciation. Such reactions can proceed in two different ways: solid-state process or coupled dissolution–reprecipitation reaction (CDRR; e.g. Putnis 2002; Xia et al. 2009). While solid-state reactions are controlled by diffusion (P, T, stress state), CDRR proceeds via the complete dissolution of the parent mineral, coupled at the nanometer scale with precipitation of the product (e.g., Putnis 2002; Xia et al. 2009). Hence, reaction kinetics is controlled by the relative solubilities of the parent and product minerals, which depends on P, T, as well as on solution chemistry (e.g., pH, redox, ligand concentrations). For example, Tenailleau et al. (2006) and Xia et al. (2008, 2009) demonstrate that the transformation of pentlandite (($Fe,Ni)_9S_8$) into violarite ($FeNi_2S_4$), which cannot be achieved at low temperature via a solid-state process, happens in a few days under mild (120°C) hydrothermal conditions following CDRR. The resulting product is characterized by high porosity, even when the product has higher molar volume than the starting material (Putnis 2002). CDRRs can proceed topotactically, preserving both the crystallographic orientation and the external shape of the replaced grain (e.g., Xia et al. 2009).

Here, we argue that the Au-rich zone II pyrite developed via the CDRR mechanism during D_{4a} and that this process may be responsible for the high Au contents in this pyrite. A good illustration that CDRRs were important in the development of the pyrite textures is provided by the crystal illustrated in Fig. 10f, which shows unambiguously that

nearly half the grain was replaced during a subsequent mineralization event; this replacement was also accompanied by an overgrowth on the original crystal. The replaced pyrite is characterized by many inclusions of arsenopyrite as well as pores. These features indicate that the replacement occurred via a CDRR, as a solid-state reaction cannot account for the sharp contact in particular. The crystal from WSZ illustrated in Fig. 10e was affected in a similar fashion by a reaction front moving through the crystal.

The features present in the crystals from Fig. 10e, f correspond to those seen in the zoned crystals in D_3 structures and in BIF (Fig. 10b–d). The Au-rich zone II is characterized by high porosity and by the presence of a myriad of micro-inclusions, which are sometimes preferentially oriented along apparent crystallographic axes of the host pyrite crystal (Fig. 10d). In conjunction with irregular boundaries between zone II and other zones, these features indicate that this zone most probably recrystallized. During this recrystallization, the original arsenian pyrite was transformed into Au-bearing arsenian pyrite with numerous arsenopyrite inclusions; Au and As were probably added to the mineral. This indicates the presence of a fluid enriched in As and Au compared to the "original" D_3 fluid. This fluid most likely corresponds to the D_{4a} fluid. The features of this recrystallization, i.e., its ability to replace specifically a particular zone in a pyrite crystal (probably characterized by a specific chemistry or microstructure), and the resulting porosity are strongly suggestive of a coupled dissolution–reprecipitation process (Putnis 2002), in which replacement occurs along a reaction front by full dissolution of the mineral followed by tightly coupled reprecipitation.

At Sunrise Dam, such coupled dissolution–reprecipitation reactions may have been important in upgrading the ore grades during D_4. This is because solution chemistry at the reaction front may be different from the conditions in the bulk of the hydrothermal fluid. As first noted by Pokrovski et al. (2002), the dissolution of As-rich pyrite (or arsenopyrite) results in the release of hydrogen:

$$FeAsS + 2Cl^- + H^+ + 3H_2O = As(OH)_3(aq) + HS^- + FeCl_2(aq) + 1.5H_2(aq)$$

This leads to reducing conditions at the reaction front, and in most cases, this is expected to decrease Au solubility (e.g., Mikucki 1998) and to favor the coprecipitation of Au with the newly formed pyrite or arsenopyrite.

Diversity of processes and protracted mineralization history

This discussion has emphasized the diversity of processes that are responsible for Au mineralization at Sunrise Dam. Thébaud et al. (2008) demonstrated the role of multiple flow via a single plumbing system in "setting the stage" for major mineralizing events. At Sunrise Dam, the D_1 and D_2 events probably contributed little to the total Au endowment,

but put in place a plumbing system that was used by all subsequent mineralization events. Alteration and low-grade mineralization during D_1 and D_2 may also have enabled more efficient transport of Au during subsequent hydrothermal events. A large portion of the gold in many orebodies was deposited during D_4. The mineralogical differences between the D_{4a} and D_{4b} stages may reflect different precipitation mechanisms from the same mineralizing fluid: fluid–rock interaction and interaction with preexisting (mainly D_3) pyrite accounting for most of the mineralization during D_{4a}, whereas D_{4b} veins probably formed from spent D_{4a} fluid (As depletion). Pressure variations during D_{4b} vein formations may have led to mineral precipitation (e.g., Liu et al. 2008), possibly facilitated by phase separation.

Such a complexity is indeed characteristic for many giant orogenic Au deposits. For example, a protracted history of Au flux leading to complex mineralization geometry and mineralogy may be the most striking feature of the giant Kalgoorlie deposit, by far the largest deposit in the Yilgarn Craton (Bateman and Hagemann 2002).

The role of sulfide recrystallization in modifying the speciation of gold (e.g., formation of visible gold from invisible gold) has long been recognized (e.g., Morey et al. 2008 and references in there). However, at Sunrise Dam, we propose a new process of Au deposition/upgrading via recrystallization following the dissolution–reprecipitation process. Given that episodic fluid flow can develop even within single mineralizing events (e.g., Sibson et al. 1988; Brugger et al. 2000, 2008), dissolution–reprecipitation reactions have the potential to play an important role in many gold deposits, and their role in the formation of giant Au deposits needs to be further investigated.

Conclusions

1. Arsenopyrite and arsenian pyrite in the Sunrise Dam gold deposit contain significant amounts of "invisible" Au; the average Au concentration is 1.61 ppm in pyrite ($n=220$) with maximum value of 3,067 ppm and 562 ppm in arsenopyrite ($n=35$) with maximum value of 5,767 ppm, which are the highest concentrations reported so far in Yilgarn Craton.

2. The presence of both native and invisible Au and high concentrations of Au in As-deficient arsenopyrite indicate that mineralization at Sunrise Dam is consistent with those of lower temperature deposits in the Yilgarn Craton and with a formation *syn*- to postgreenschist facies peak metamorphism (Mair et al. 2000).

3. Our dataset shows few systematic differences among pyrite crystals from different stages, apart from D_{4a} showing the highest Au and Te contents (Figs. 6 and 8). The highest Au values (both average and maximum) are

obtained from D_{4a} stage pyrite and arsenopyrite, which is consistent with D_{4a} being the major mineralizing event in the deposit. The elevated Cr–Ni–Co signature in some pyrite assemblages reflects their crystallization in rock of (ultra-) mafic affinity and pronounced fluid–rock interaction. Similarly, some locally high Bi contents may reflect mobilization of Bi from intermediate volcanics during fluid–rock interaction.

4. The sulfidation of BIF originally produced Au-poor pyrite (<0.4 ppm). Upgrading of Au contained in BIF pyrite was partly the result of a *coupled dissolution–reprecipitation reactions* during the D_{4a} stage. A similar mechanism also upgraded the Au contents in vein-hosted D_3 pyrites. Textures indicative of *coupled dissolution–reprecipitation reactions* are common in the deposit and may account for a significant increase in Au grades during D_{4a}. The importance of coupled dissolution–reprecipitation as a Au-enrichment factor in polystage hydrothermal ore deposits has not been previously recognized, but such reactions have a large potential for efficiently scavenging Au from a hydrothermal fluid, by creating locally highly reducing conditions.

5. Recrystallization of pyrite also resulting in altering Au speciation in the deposit. D_{4b}-stage pyrite contains a significant amount of Au as inclusions of Au–tellurides (e.g., nagyágite). This pyrite also contains numerous inclusions of native gold, which resulted from the expulsion of lattice-bound Au, its micrometer-scale remobilization and redeposition during a late post-D_{4b} event. Further evidence for postcrystallization remobilization of Au in pyrite is provided by the presence of metallic Au below the gold solubility limit of Reich et al. (2005) in D_3 and D_{4b} arsenian pyrite, resulting from remobilization during the D_{4a} and D_{4b} stages.

6. The textures and chemistry of pyrite and arsenopyrite provide insights about mineralization processes. The complex speciation of Au at Sunrise Dam results from the large variety of mineralization processes that were responsible for Au precipitation (fluid–rock interaction with different rocks; possibly phase separation; dissolution–reprecipitation reactions) as well as postcrystallization remobilization. Such a complexity is indeed characteristic for many giant orogenic Au deposits (e.g., Bateman and Hagemann 2002; Mumin et al. 1994) and reflects multiple fluid flow through a single plumbing system.

Appendix

Table 4 LA-ICP-MS analyses of pyrite in the Sunrise Dam gold deposit

Spot no	Stage	Cr	Co	Ni	Cu	As	Ag	Sb	Te	Au	Pb	Bi
S7-2-1	D_1	12.0	584	504	4,589	737	43.4	1,276	1.17	1.79	137	141
S7-2-2		35.9	410	268	292	552	1.73	13.6	1.75	<0.3	49.9	36.4
S7-2-3		61.3	1,450	528	1,546	3,326	10.8	177	3.01	6.56	117	91.7
S7-2-4		<3.9	867	482	1,534	404	12.5	362	1.54	<0.3	87.2	72.3
S7-2-5		<8.4	2,122	1,458	411	1,546	15.8	127	2.96	1.82	101	73.3
S7-2-6		35.5	3,245	924	46,633	15,099	24.1	1,959	4.07	4.02	1,040	261
C4-2-1	D_3	<1.9	667	2,606	3.70	13.7	<0.0	<0.1	<0.4	<0.0	0.08	<0.0
C4-2-11		79.3	157	2,134	313	17,184	14.5	60.7	92.8	25.8	190	35.2
C4-2-12		<131	25.1	19,610	4,507	25,938	3,310	662	81.2	19.5	761	236
C4-2-2		<1.9	469	1,646	2.24	17.3	0.09	<0.0	14.7	<0.0	7.32	12.0
C4-2-3		<1.9	1,528	1,426	4.46	8.06	0.12	<0.0	4.09	<0.0	1.19	4.79
C4-2-7		<2.5	12,725	1,218	106	1,604	2.84	14.3	9.79	6.86	15.8	4.88
C4-2-8		<1.9	28.5	4,649	1,603	113	1.85	0.84	2.04	0.20	6.82	5.77
GQ1-13-1		14.9	19.1	75.2	90.3	789	3.08	2.65	6.85	2.28	29.9	1.95
GQ1-13-2		23.1	5.63	41.9	18.1	142	0.46	3.23	2.88	0.08	30.1	0.14
GQ1-13-3		2.89	557	316	159	270	3.83	9.42	5.06	1.03	68.9	3.36
GQ1-13-4		<3.6	3.82	62.7	2.56	665	0.27	<0.2	0.78	0.24	0.70	0.05
GQ1-13-5		<4.6	26.6	180	4.51	381	0.50	0.52	1.72	0.27	0.87	0.05
GQ1-4-1		<9.1	859	185	35,783	9,865	42.8	3,106	1.66	0.98	20.5	130
GQ1-4-2		22.6	371	78.6	558	334	0.84	12.8	<1.3	0.21	21.8	6.04
GQ1-4-3		<2.0	38.5	51.5	145	13,862	0.29	60.8	0.42	3.29	2.06	2.42
GQ1-4-4		76.0	478	147	2,007	5,204	2.49	68.3	2.16	1.54	19.0	13.2
GQ1-4-5		<6.1	188	66.2	4,607	1,147	10.8	862	2.09	0.37	10.2	16.1
GQ1-4-6		28.8	361	418	4,271	4,339	5.59	346	1.36	2.20	16.8	91.8
GQ1-4-7		44.2	1,765	540	406	12,224	5.86	227	15.4	4.80	254	88.6
GQ1-4-8		15.5	1,648	388	214	11,124	3.54	68.4	14.7	3.24	172	57.9
GQ1-4-9		23.7	417	196	1,369	22,101	3.46	78.0	2.92	3.10	32.7	20.3
GQ1-9-1		1.7	31.4	122	8.92	5,549	0.15	0.38	0.82	1.13	2.54	0.08
GQ1-9-2		36.6	66.3	593	3.16	10,663	<0.0	0.21	<0.3	0.41	0.15	<0.0
GQ1-9-3		12.4	56.7	243	11.1	21.0	0.12	6.03	0.41	<0.0	5.73	0.52
GQ1-9-4	D_3	<1.7	25.6	104	7.83	13,548	0.15	3.19	0.73	1.74	3.87	0.35
GQ1-9-5		<11	28.7	71.6	78.5	78.1	0.66	<0.4	<2.1	<0.4	2.05	<0.1
Mg8-1-1		<1.3	305	261	2.59	95.3	2.57	1.70	4.06	0.54	68.3	74.8
Mg8-1-2		3.10	519	399	7.69	610	0.69	0.70	8.91	0.59	25.1	18.3
Mg8-1-3		2.13	247	418	37.4	203	0.54	2.32	1.78	0.27	55.8	13.6
Mg8-1-4		20.5	206	1,518	1.68	216	0.85	1.95	1.46	0.29	24.0	10.4
Mg8-1-5		18.1	362	325	386	530	4.13	3.90	12.9	2.37	192	112
Mg8-1-6		3.88	292	338	18.4	1,080	3.02	2.82	13.4	1.17	105	97.3
S311-1		165	172	1,150	216	1,634	5.85	55.1	2.34	1.79	515	13.6
S311-2		<16	91.8	604	33.7	355	1.62	25.7	<0.8	<0.3	473	6.39
S311-3		12.1	13.5	92.6	1,199	18,792	1.66	11.9	<0.2	0.34	27.6	0.97
S311-4		<2.3	18.9	915	8,202	16,463	6.95	21.0	0.45	3.02	36.0	1.85
S311-5		<2.3	20.4	573	20.8	8,625	1.40	1.20	1.02	0.33	25.2	2.48
S313-1		3.53	12.8	94.2	95.2	26,092	1.19	7.84	2.98	1.94	33.4	1.60
S313-2		<2.5	6.14	66.0	3.99	143	<0.0	<0.1	<0.2	<0.0	0.08	<0.1
S313-3		<13	<0.8	20.8	17.1	27,298	0.32	1.94	4.10	<0.1	5.43	0.20
S313-4		3.07	14.6	131	2,505	9,196	16.9	170	25.6	13.8	174	9.40

Table 4 (continued)

Spot no	Stage	Cr	Co	Ni	Cu	As	Ag	Sb	Te	Au	Pb	Bi
S313-5	D_3	8.58	9.28	181	442	7,650	4.50	22.7	10.3	4.85	50.1	2.40
S313-6		<2.4	2.43	46.0	3.26	95.9	<0.0	<0.1	0.37	<0.0	0.68	<0.1
S313-7		<2.4	21.0	85.4	1,405	4,747	7.29	52.7	15.5	11.2	491	5.53
S313-8		<2.2	20.5	235	11.1	7,911	1.97	1.81	10.3	0.75	23.0	2.08
SU2-1		<0.9	748	1,238	1.13	915	<0.1	<0.1	<0.7	0.04	0.31	0.06
SU2-2		<2.7	845	826	<3.0	383	<0.2	0.20	<2.8	<0.1	0.22	0.07
SU2-3		<1.9	478	578	<2.4	919	<0.1	<0.1	<2.2	0.13	0.57	0.18
SU2-4		2.42	338	981	52.9	634	1.14	1.73	7.60	0.48	16.4	2.60
SU11-2		<3.0	1.60	4.77	<4.8	3,709	<0.2	<0.3	<2.9	0.38	0.74	0.06
SU17-1		6.28	9.43	28.3	<4.0	1,491	<0.2	1.28	<2.0	0.38	3.71	0.73
SU11-3		6.04	27.9	77	8.49	8.44	0.69	2.20	<2.5	<0.1	9.98	6.46
SU17-5		<2.6	16.0	55.2	51.5	79.4	<0.2	1.77	<2.7	0.23	13.4	3.97
A3-1	D_{4a}	25.2	54.4	1,644	4,191	11,843	11.6	178	16.9	8.54	83.0	5.34
A3-2		30.7	87.5	599	7,476	10,274	18.1	359	116	46.4	155	9.58
A3-3		3.74	53.6	351	1,325	8,774	25.2	194	134	135	112	6.78
A3-4		6.51	18.9	303	1,060	9,456	13.9	98.0	179	75.8	166	9.49
A3-5		<2.0	65.9	385	11.7	522	3.07	<0.1	<0.6	1.67	0.84	0.02
A3-6		9.53	18.5	205	3,152	10,860	28.2	182	267	166	221	13.0
A4-1		<6.1	94.9	135	47.6	1,198	0.58	5.21	<1.9	24.1	7.49	1.88
A4-2		5.37	39.5	401	5,639	14,247	15.6	619	254	79.8	309	2.79
A4-3		5.51	71.3	416	1,630	23,010	14.5	111	214	132	169	4.45
A4-4		5.80	30.1	356	1,009	9,232	23.8	160	266	126	100	3.32
A4-5		51.6	42.9	357	440	10,067	24.9	106	538	110	293	3.56
A4-6		17.4	26.1	311	493	54,860	5.49	188	38.9	53.9	204	2.59
C4-2-10		235	524	3,201	755	5,420	5.01	122	25.0	23.0	50.4	33.9
C4-2-4		2,271	456	4,309	4,346	15,172	53.7	1,972	219	62.5	224	53.3
C4-2-5		245	64.2	687	<2.5	4,165	0.36	2.50	6.95	1.01	25.6	1.71
C4-2-6		201	78.4	3,244	171	13,354	19.8	40.1	115	24.4	73.7	41.5
C4-2-9		3,924	153	4,117	2,447	13,928	39.0	190	235	133	131	41.5
C4-6-1		325	1,019	1,935	123	16,904	1.31	11.9	15.4	136	51.4	16.9
C4-6-2		<1.9	742	546	6.32	58.6	0.09	4.66	0.47	0.21	4.42	0.51
C4-6-3		30.7	3,149	1,434	168	2,058	2.08	25.3	3.25	3.17	73.1	14.6
C4-6-4		<2.0	2.39	213	1,707	2,800	0.78	16.0	0.97	1.00	27.4	1.87
C4-6-5		123	243	1,727	171	9,977	6.31	26.4	21.6	12.9	117	15.7
C4-6-6		<4.4	201	1,816	3,141	28,204	83.5	1,201	71.6	97.9	228	27.7
C4-6-7		<18	360	2,356	16.5	10,961	<1.0	9.36	9.46	28.7	34.9	6.37
Dp6-1-1		2.71	112	606	129	35,494	8.06	255	50.4	133	406	78.1
Dp6-1-2		31.5	69.1	214	67.5	7,517	17.3	116	12.0	27.3	2,438	149
Dp6-1-3		25.1	66.0	289	38.2	1,142	3.76	26.5	9.58	10.4	135	246
Dp6-2-1		6.90	534	819	477	636	13.9	207	20.8	3.14	1,745	97.5
Dp6-2-2		25.3	82.4	247	215	731	7.30	286	3.34	1.32	722	76.8
Dp6-2-3		112	353	532	164	3,309	3.93	612	6.55	1.40	354	55.8
Dp6-2-4		2.78	133	169	13.1	107	1.70	49.4	5.54	0.47	65.7	81.4
Dp6-2-5		<1.4	0.17	58.3	1.85	402	0.25	3.74	1.67	0.46	34.8	6.94
Dp6-2-6		<1.4	78.8	53.5	39.0	6,811	1.54	14.7	252	55.4	308	5.64
Dp6-2-7		128	105	246	34.0	2,038	3.84	48.5	17.9	2.42	388	31.4
Dv5-1-1		<1.9	800	223	19.7	108	0.52	15.7	10.9	0.56	194	21.7
Dv5-1-2		3.62	78.0	216	1,027	411	7.81	291	15.6	1.82	75.8	43.0
Dv5-1-3		<2.0	2.21	127	177	102	0.81	2.31	65.9	0.18	9.07	27.2

Table 4 (continued)

Spot no	Stage	Cr	Co	Ni	Cu	As	Ag	Sb	Te	Au	Pb	Bi
Dv5-1-4	D$_{4a}$	3.33	202	823	12.2	270	0.74	10.3	7.51	0.70	54.7	68.1
Dv5-1-6		18.4	165	626	1,316	6,957	10.4	415	<0.4	2.18	92.5	10.8
GQ1-6-1		<8.1	327	153	5,003	66,819	9.14	167	13.9	43.7	75.2	8.28
GQ1-6-2		<7.7	376	287	47.7	612	0.21	0.90	<1.7	0.17	7.06	0.18
GQ1-6-3		<2.4	733	408	6,081	17,921	9.26	152	8.86	11.2	105	5.11
GQ1-6-4		<2.4	216	130	5,866	38,177	27.4	110	2.35	98.3	51.9	1.49
GQ1-6-5		<8.0	69.0	17.6	915	1,481	1.76	41.3	<1.5	11.7	21.6	0.33
GQ1-6-6		<8.7	111	22.5	273	29,709	1.32	24.3	16.8	44.5	37.1	3.13
GQ1-9-6		24.3	29.3	234	2,795	13,588	2.98	15.1	<1.2	0.75	126	1.11
GQ1-9-7		<3.7	29.6	269	21.7	19,884	<0.1	3.19	<1.0	1.20	1.46	0.06
GQ1-9-8		<5.1	53.7	845	3.43	981	0.17	0.43	2.10	<0.2	1.64	0.41
Mg8-3-1		14.4	448	241	661	40.5	1.35	7.28	2.63	0.77	179	17.2
Mg8-3-2		<1.1	314	887	3.42	98.5	<0.0	<0.1	<0.2	<0.1	0.21	0.22
Mg8-3-3		18.5	537	368	3,471	1,495	4.19	60.9	4.90	5.96	427	21.6
Mg8-3-4		63.5	1,787	759	1,822	1,803	11.2	153	15.7	4.18	2,364	89.2
Mg8-3-5		<0.9	152	914	2.56	29.1	<0.0	<0.1	0.32	<0.0	1.17	0.21
Mg8-3-6		29.2	175	246	13,653	1,598	7.46	54.9	3.84	4.26	538	40.1
Mg8-3-7		11.3	225	853	20.0	789	0.52	9.52	0.84	0.17	97.4	3.34
Mg8-3-8		13.6	1,565	836	8.52	177	0.24	4.89	1.04	0.20	11.8	3.25
Mg8-3b-1		1.34	626	145	3.78	81.7	1.34	2.91	1.61	0.28	586	19.7
Mg8-3b-2		<1.4	115	132	6.45	132	0.74	1.55	0.89	0.16	20.3	19.3
Mg8-3b-3		<1.3	366	825	2.20	170	0.12	0.51	0.33	<0.1	1.32	0.79
Mg8-3b-4		2.07	748	553	1,859	147	5.54	11.6	9.86	1.26	394	172
Mg8-3b-5		1.45	1,160	336	14.7	1,434	0.17	0.84	2.74	0.31	23.4	0.36
Mg8-3b-6		1.32	210	1,115	162	215	0.93	1.90	5.12	0.63	91.7	15.2
Mk2-1-1		<10	3,152	3,234	5,163	3,123	36.2	877	11.7	11.1	223	22.6
Mk2-1-2		<9.7	271	2,696	<1.3	3,155	<0.1	0.58	0.93	0.20	1.75	<0.1
Mk2-1-3		26.5	171	1,786	38.6	4,352	<0.1	7.57	30.8	9.99	19.3	0.30
Mk2-1-4		<15	34.9	152	130	10,226	3.81	21.2	35.7	73.6	57.5	1.75
Mk2-1-5		<13	89.1	387	93.6	2,430	3.35	13.8	23.2	14.2	57.4	2.34
Mk2-1-6		<11	214	2,334	1.47	2,965	0.93	<0.2	1.58	<0.1	3.84	0.23
Mk2-1-7		35.8	88.8	606	6.41	962	<0.1	5.20	9.76	0.92	13.8	0.34
WSZ-15-1		10.2	438	9,401	8,892	29,579	91.6	2,736	82.6	73.3	3,638	779
WSZ-15-10		303	5,606	985	327	12,399	5.41	154	54.1	33.6	2,003	2,180
WSZ-15-11		67.3	614	506	213	793	4.97	11.7	37.9	2.88	608	1,772
WSZ-15-2		49.0	111	857	239	19,466	52.6	17.9	4.60	315	211	46.1
WSZ-15-3		<2.7	94.3	3,471	355	19,959	15.1	36.5	7.65	540	213	41.8
WSZ-15-4		<2.3	6.70	4,070	0.54	2,857	0.10	<0.2	0.49	0.17	6.76	2.92
WSZ-15-5		<1.4	160	5,530	1,620	17,356	549	351	184	210	1,772	999
WSZ-15-6		<1.4	74.2	1,399	1,173	12,841	201	250	182	411	1,453	923
WSZ-15-7		9.86	1,878	25,699	962	58,720	1,564	105	140	3,067	6,090	1,563
WSZ-15-8		31.7	1,117	2,624	210	12,309	2.58	39.9	18.5	126	365	81.3
WSZ-15-9		<3.9	1,098	2,274	425	14,816	4.88	6.06	28.6	269	181	282
SU17-2		17.6	2.38	9.78	35.9	28,089	<0.3	4.03	34.6	148	8.70	0.25
SU17-3		<3.6	5.62	22.1	12.4	22,431	<0.3	3.41	<2.3	4.01	3.90	0.06
SU17-4		<2.4	0.53	1.69	<3.6	19,353	<0.3	0.41	<2.6	3.97	1.36	0.10
SU17-6		<2.3	17.0	31.6	<4.1	11,254	<0.2	3.79	<2.1	3.86	17.4	0.59
SU17-7		<3.2	<0.1	<0.7	5.83	16,988	<0.2	1.13	<2.5	0.96	1.58	<0.0
GQ19-1-1		<3.0	108	2,961	4.74	1,015	<0.1	<0.1	<1.9	<0.0	0.05	0.03

Table 4 (continued)

Spot no	Stage	Cr	Co	Ni	Cu	As	Ag	Sb	Te	Au	Pb	Bi
GQ19-1-2	D_{4a}	92.9	473	7,474	29.9	6,489	0.21	0.63	3.78	1.16	2.20	0.52
GQ19-1-3		<1.9	537	2,252	<2.8	2,226	0.25	<0.2	<1.9	0.11	0.06	0.03
GQ19-1-4		78.7	212	1,911	416	138	0.26	0.47	<1.8	<0.0	1.74	11.8
GQ19-1-5		<2.2	150	2,679	<2.7	3,888	0.22	<0.1	3.63	0.28	0.37	0.36
GQ19-1-6		73.9	144	5,057	3.86	6,369	0.66	2.24	16.3	0.77	16.5	1.36
GQ19-1-7		7.40	130	4,884	3.74	6,520	1.43	1.06	21.3	2.13	15.5	1.63
GQ19-2-1		<3.5	42.3	946	202	659	2.83	1.08	15.1	22.4	11.9	0.82
GQ19-2-2		<3.3	1.55	67.5	<5.3	80.4	<0.4	<0.2	<2.5	<0.1	0.14	<0.0
WSZ333-1		5.29	18.5	205	112	4,859	0.96	34.6	<1.5	0.98	14.6	0.13
WSZ333-2		<2.3	18.8	274	<3.1	823	<0.3	0.22	<2.3	<0.1	0.85	<0.0
WFZ311-1		<2.9	47.0	1,057	1,393	297	4.04	2.21	4.22	0.42	33.0	11.3
WFZ311-2		<1.7	0.53	59.7	4,200	17,568	0.35	0.52	<1.5	45.2	18.2	<0.0
WFZ312-1		<0.6	139	157	0.60	314	<0.0	0.02	85.1	<0.0	<0.0	<0.0
WFZ312-2		<1.7	1.00	4.11	<2.5	217	<0.1	0.22	<2.2	<0.1	0.11	0.08
WFZ312-3		<1.7	688	39.1	19.3	346	0.32	1.40	5.07	0.26	15.7	8.31
WFZ312-4		<1.6	1,892	72.8	<2.4	388	<0.1	<0.1	97.6	<0.1	1.25	2.20
WFZ312-5		<2.0	159	14.5	<2.3	264	<0.2	<0.1	71.3	<0.0	0.90	1.23
WFZ312-6		1.01	27.1	92.1	6.21	985	0.54	1.13	25.3	0.85	15.1	11.4
Dv5-2a-1	D_{4b}	156	148	906	12,458	7,798	20.4	2,167	3.81	3.02	262	43.3
Dv5-2a-2		439	85.0	764	321	3,019	4.71	1,244	2.21	1.95	162	26.2
Dv5-2a-3		2.52	643	2,858	<0.6	4,131	<0.0	<0.2	<0.4	<0.0	0.14	0.05
Dv5-2a-4		143	7.39	257	1,462	2,858	18.9	2,004	1.74	2.69	116	32.6
Dv5-2a-5		55.9	57.8	898	27,296	14,908	58.3	2,453	4.18	4.50	187	58.5
Dv5-2a-6		4.68	18.2	1,610	29.6	2,941	1.24	9.77	1.01	0.95	40.2	8.48
Dv5-2a-7		4.50	12.5	353	99.4	2,917	0.64	117	<0.5	0.63	36.6	0.62
GQ1-10-1		<3.9	31.5	204	41.1	48.8	0.19	0.20	<1.0	<0.2	0.84	0.25
GQ1-10-2		<2.0	40.7	431	445	423	0.67	2.79	1.61	0.19	6.82	1.86
GQ1-10-3		<2.5	15,640	1,347	3.75	115	0.27	0.28	1.23	0.24	5.90	16.8
GQ1-1-1		<1.9	2.68	29.6	28.1	5,574	0.17	0.42	11.7	2.62	2.90	0.08
GQ1-1-10		1.87	2.12	11.8	263	11,157	0.66	44.9	2.29	9.35	9.46	0.49
GQ1-1-11		33.9	73.4	202	12,869	5,708	74.4	5,256	23.6	13.7	52.7	3.12
GQ1-1-12		109	73.7	429	132	16,416	0.41	23.6	5.25	15.2	36.0	1.66
GQ1-1-13		<6.1	232	590	145	4,646	1.29	5.94	17.3	1.07	18.8	1.89
GQ1-1-14		<1.3	50.0	62.6	26.9	19,342	<0.0	0.50	2.05	2.00	0.65	0.01
GQ1-1-15		4.50	373	1,030	10.3	2,033	0.44	1.96	4.02	0.37	10.2	1.03
GQ1-1-16		<10	280	1,017	15.8	1,531	0.19	2.04	3.00	<0.3	26.0	1.00
GQ1-1-2		<1.4	1.54	27.1	85.4	10,909	0.03	0.18	16.6	7.03	1.03	0.02
GQ1-1-3		<1.4	11.7	223	23.0	16,216	<0.0	0.48	52.9	5.38	0.79	<0.0
GQ1-1-4		<1.5	1.12	7.69	13.7	12,802	<0.0	0.51	38.9	2.91	0.79	<0.0
GQ1-1-5		<2.1	0.11	1.27	28.1	10,104	0.04	0.38	29.5	5.43	0.67	<0.0
GQ1-1-6		<2.3	1.01	11.4	21.3	11,225	<0.0	<0.1	27.6	2.67	0.04	<0.0
GQ1-1-7		<1.6	0.09	2.94	665	9,399	0.75	7.68	12.5	3.38	16.7	0.26
GQ1-1-8		<1.4	0.88	5.41	142	15,306	0.04	0.18	8.91	15.8	0.31	0.02
GQ1-1-9		<2.4	9.21	129	21.9	8,186	0.11	3.89	20.8	2.84	8.84	0.08
GQ1-2a-1		<2.4	545	62.1	9.69	675	0.08	<0.1	<0.5	0.13	0.11	0.03
GQ1-2a-2		<1.7	178	203	2.17	142	<0.0	<0.0	<0.4	0.07	0.58	0.50
GQ1-2a-3		<1.7	603	35.0	3.44	412	<0.0	<0.0	1.17	0.15	0.45	0.50
GQ1-2a-4		3.35	310	83.4	1.60	20.4	<0.1	<0.1	48.2	<0.0	<0.0	<0.0
GQ1-2a-5		3.09	412	56.8	9.36	246	1.30	0.84	42.8	0.22	4.58	17.8

Table 4 (continued)

Spot no	Stage	Cr	Co	Ni	Cu	As	Ag	Sb	Te	Au	Pb	Bi
GQ1-2a-6	D$_{4b}$	<2.4	292	45.8	4.67	381	0.06	<0.1	<0.5	<0.0	0.09	0.08
GQ1-2a-7		<2.3	63.4	6.42	5.78	276	<0.0	<0.1	0.47	<0.0	0.23	0.06
Mg-1-1		1.89	7.58	43.5	19.9	2,217	2.89	6.55	6.53	4.07	97.8	51.8
Mg-1-2		1.48	3.23	45.5	175	204	1.28	5.60	0.76	0.26	21.1	5.83
Mg-1-3		3.08	1,454	176	23.6	428	0.68	13.7	0.86	0.44	53.3	24.5
Mg-1-4		5.81	414	686	12.6	456	568	21.5	4.74	1.35	77.4	13.9
Mg-1-5		<1.3	1.95	50.4	8.90	657	2.05	0.55	2.24	4.30	6.15	4.66
Mg8-6-1		<1.4	443	292	1.30	15.5	<0.1	<0.1	1.75	<0.1	0.32	1.68
Mg8-6-2		6.23	316	1,138	12.2	318	0.84	3.05	5.16	0.61	64.2	82.1
Mg8-6-3		<1.4	53.0	61.5	2.00	1,543	0.09	0.36	9.66	0.82	9.27	2.91
Mg8-6-4		1.66	283	966	454	1,307	3.55	26.5	17.1	7.95	280	110
Mg8-6-5		1.06	51.7	568	17.7	318	0.28	4.42	6.37	0.33	57.0	29.1
Mg8-6-6		2.22	128	1,122	113	394	1.02	11.5	6.86	2.15	158	64.7
Mg8-6-7		1.02	14.0	985	5.69	470	0.25	0.77	1.93	0.54	14.9	21.1
Mk2-2-1		1.99	119	2,180	33.9	3,704	1.53	980	6,426	140	5,751	18.3
Mk2-2-2		<2.0	0.47	28.7	2.20	2,080	2.49	314	842	290	1,925	5.95
Mk2-2-3		3.09	73.8	1,188	4.23	926	<0.0	<0.1	11.1	<0.0	0.29	<0.0
Mk2-2-4		34.8	10.4	344	997	19,534	119	134	499	215	277	13.5
Mk2-2-5		<1.8	59.9	1,084	50.1	3,713	1.85	1.83	49.1	9.14	21.2	2.45
SU4-1		0.74	101	319	4.23	922	0.41	17.4	53.3	18.2	115	1.21
SU4-2		26.7	194	601	5.57	996	0.19	4.28	2.22	0.52	27.9	2.13
SU10-2		2.11	112	351	2.60	5,053	<0.0	1.17	7.13	2.32	4.08	0.05
SU5-1		3.43	234	1,064	12.3	857	1.17	1.32	4.33	0.49	4.00	0.34
SU5-2		<1.2	0.79	21.2	5.65	888	61.0	0.89	54.9	10.1	12.0	4.64
SU5-3		<1.0	0.20	11.8	<1.5	1,384	<0.1	<0.0	<0.9	<0.0	0.06	<0.0
SU5-4		<1.2	<0.0	12.2	74.8	1,510	<0.1	0.13	1.38	0.16	0.30	<0.0
SU15-2-1		<1.4	0.10	974	3.69	1,282	<0.1	<0.0	<0.5	<0.0	<0.0	<0.0
SU15-2-2		<1.0	0.39	4.83	<1.2	4,426	<0.1	<0.0	<0.8	<0.0	0.03	<0.0
SU15-2-3		60.9	233	1,103	90.8	567	14.00	9.88	38.1	9.75	2,130	4.65
SU15-2-4		<2.6	111	1,521	23.8	764	19.14	0.67	32.6	15.0	5.43	0.08
SU11-(magnetite)		<1.4	4.12	157	<11	10.0	<1.1	0.70	<0.8	<0.4	<0.2	<0.1

Data in parts per million

SU7 SSZ open pit, *C4* Cosmo 1940OD, *GQ1* GQ open pit, *Mg8 and Mg-1* Margies open pit, *S311 and S313* SSZ 2075OD, *SU2 SU4, SU10, SU5 and SU11* SSZ 2077OD, *SU17 and SU5* SSZ 2067OD, *A3 and A4* Astro core UGD728, *Dp6* Dolly Porphyry 1930OD, *Dv5* Dolly Volcanic 1931OD, *Mk2* Mako 2087OD, *WSZ-15 and WSZ333* WSZ open pit S wall, *GQ19* GQ 1960OD, *WFZ311 and WFZ312* WFZ open pit SE wall

References

Arehart GB, Chryssoulis SL, Kesler SE (1993) Gold and arsenic in iron sulfides from sediment-hosted disseminated gold deposits: implication for depositional processes. Econ Geol 88:171–185

Ashley PM, Creagh CJ, Ryan CG (2000) Invisible gold in ore and mineral concentrates from the Hillgrove gold-antimony deposits, NSW, Australia. Miner Depos 35:285–301

Bateman R, Hagemann S (2002) Gold mineralisation throughout about 45 Ma of Achaean orogenesis: protracted flux of gold in the Golden Mile, Yilgarn Craton, Western Australia. Miner Depos 39:536–559

Brown SM, Groves DI, Newton PJN (2002) Geological setting and mineralization model for the Cleo gold deposit, Eastern Goldfields Province, Western Australia. Miner Depos 37:704–721

Brown SM, Johnson CA, Watling RJ, Premo WR (2003) Constraints on the composition of ore fluids and implications for mineralising events at the Cleo gold deposit, Eastern Goldfields Province, Western Australia. Aust J Earth Sci 50:19–38

Brugger J, Lahaye Y, Costa S, Lambert D, Bateman R (2000) Inhomogeneous distribution of REE in scheelite and dynamics of Archaean hydrothermal systems (Mt. Charlotte and Drysdale gold deposits, Western Australia). Contrib Mineral Petrol 139:251–264

Brugger J, Etschmann B, Pownceby M, Liu W, Grundler P, Brewe D (2008) Tracking the chemistry of ancient fluids: oxidation state

of europium in hydrothermal scheelite. Chem Geol 257:26–33. doi:10.1016/j.chemgeo.2008.08.003

Cabri LJ, Chryssoulis SL, DeVilliers JPR, Laflamme JHG, Buseck PR (1989) The nature of "invisible" gold in arsenopyrite. Can Mineral 27:353–362

Cassidy KF, Champion DC, Fletcher IR, Dunphy JM, Black LP, Claoue-Long JC (2002) Geochronological constraints on the Leonora-Laverton transect area, north eastern Yilgarn Craton. In: Cassidy KF (ed) Geology, geochronology and geophysics of the north eastern Yilgarn Craton, with an emphasis on the Leonora-Laverton transect area. Geoscience Australia, Record 2002/18. Geoscience Australia, Symonston, ACT, pp 31–50

Cathelineau M, Boiron MC, Holliger P, Marion P, Denis M (1989) Gold in arsenopyrite: crystal chemistry, location and state, physical and chemical conditions of deposition. In: Keays R, Skinner BJ (eds) Source, transport and deposition of metals. Econ Geol Monograph 6. Balkema, Rotterdam, pp 328–341

Ciobanu CL, Gabudeanu B, Cook NJ (2004) Neogene ore deposit and metallogeny of the Golden Quadrilateral, south Apuseni Mountains, Romania. Guidebook of the international field workshop of IGCP project 486, Alba Iulia, Romania, 31 Aug–7 Sep

Ciobanu CL, Cook NJ, Pring A, Brugger J, Danyushevsky L, Shimizu M (2009) 'Invisible gold' in bismuth chalcogenides. Geochim Cosmochim Acta 73:1970–1999. doi:10.1016/j.gca.2009.01.006

Coleman LC (1957) Mineralogy of the giant Yellowknife gold mine, Yellowknife, N.W.T. Econ Geol 52:400–425

Cook NJ, Chryssoulis SL (1990) Concentration of "Invisible gold" in the common sulfides. Can Mineral 28:1–16

Danyushevsky L, Robinson P, McGoldrick P, Large R, Gilbert S (2003) LA-ICPMS of sulphides: evaluation of an XRF glass disc standard for analysis of different sulphide matrixes. Geochim Cosmochim Acta 67:A73

Fleet ME, Mumin H (1997) Gold-bearing arsenian pyrite and marcasite and arsenopyrite from Carlin Trend gold deposits and laboratory synthesis. Am Mineral 82:182–193

Fleet ME, Chryssoulis SL, MacLean PJ, Davidson R, Weisener CG (1993) Arsenian pyrite from gold deposits: Au and As distribution investigated by SIMS and EMP, and color staining and surface oxidation by XPS and LIMS. Can Mineral 31:1–17

Genkin AD, Bortnikov NS, Cabri LJ, Wagner FE, Stanley CJ, Safonov YG, McMahon G, Friedl J, Kerzin AL, Gamyanin GN (1998) A multidisciplinary study of invisible gold in arsenopyrite from four mesothermal gold deposits in Siberia, Russian Federation. Econ Geol 93:463–487

Hallberg JA (1985) Geology and mineral deposits of Leonora-Laverton Area, northeastern Yilgarn Block, Western Australia. Hesperian, Victoria Park, Western Australia, p 140

Johan Z, Marcoux E, Bonnemaison M (1989) Arsénopyrite aurifère: mode de subsitution de Au dans la structure de FeAsS. C R Acad Sci (Paris) 308:185–191

Larocque ACL, Hodgson CJ, Cabri LJ, Jackman JA (1995) Ion-microprobe analysis of pyrite, chalcopyrite and pyrrhotite from the Mobrun VMS deposit in northwestern Quebec: evidence for metamorphic remobilization of gold. Can Mineral 33:373–388

Lentz DR (2002) Sphalerite and arsenopyrite at the Brunswick No. 12 massive sulfide deposit, Bathurst camp, New Brunswick: constraints on P-T evolution. Can Mineral 40:19–31

Liu W, Brugger J, Etschamnn B, Testemale D, Hazemann JL (2008) The solubility of nantokite (CuCl$_{(s)}$) and Cu speciation in low density fluids near the critical isochore: an in-situ XAS study. Geochim Cosmochim Acta 72:4094–4106

Maddox LM, Bancroft GM, Scaini MJ, Lorimer JW (1998) Invisible gold: comparison of Au deposition on pyrite and arsenopyrite. Am Mineral 83:1240–1245

Mair JL, Ojala VJ, Salier BP, Groves DI, Brown SM (2000) Application of stress mapping in cross-section to understanding ore geometry, predicting ore zones and development of drilling strategies. Aust J Earth Sci 47:895–912

McClenaghan SH, Lentz DR, Cabri LJ (2004) Abundance and speciation of gold in massive sulfides of the Bathurst mining camp, New Brunswick, Canada. Can Mineral 42:851–871

Mernagh TP, Heinrich CA, Mikucki EJ (2004) Temperature gradients recorded by fluid inclusions and hydrothermal alteration at the Mount Charlotte gold deposit, Kalgoorlie, Australia. Can Mineral 42:1383–1403

Mikucki EJ (1998) Hydrothermal transport and depositional processes in Archean lode-gold systems: a review. Ore Geol Rev 13:307–321

Morey AA, Tomkins AG, Bierlein FP, Weinberg RF, Davidson GJ (2008) Bimodal distribution of gold in pyrite and arsenopyrite: examples from the Archean Boorara and Bardoc shear systems, Yilgarn Craton, Western Australia. Econ Geol 103:599–614

Mumin AH, Fleet ME, Chryssoulis SL (1994) Gold mineralization in As-rich mesothermal gold ores of the Bogosu–Prestea mining district of the Ashanti Gold Belt, Ghana: remobilization of "invisible" gold. Miner Depos 29:445–460

Neumayr P, Cabri LJ, Groves DI, Mikucki EJ, Jackman JA (1993) The mineralogical distribution of gold and relative timing of gold mineralization in two Archean settings of high metamorphic grade in Australia. Can Mineral 31:711–725

Newton PGN, Tornatora PMA, Smith R, Clifford M (2002) The Cleo-Sunrise Au deposit, Laverton, WA: contrasting structural styles within a thrust duplex. In: Vearncombe S (ed) Applied structural geology for mineral exploration and mining. International Symposium, Abstract Volume. Aust Inst Geosci Bull 36. Australian Institute of Geoscientists, Perth Business Centre, WA, pp 152–155

Nugus M, Blenkinsop T, Biggam J, Doyle M (2005a) The role of early-formed structure in lode gold mineralisation: the Sunrise Dam gold Mine, Yilgarn Craton, WA. In: Hancock H et al (eds) Best practice and innovation in global mine geology, 29 May–3 June. Publication 64. Economic Geology Research Unit, School of Earth Sciences, James Cook University, Townsville, Queensland, p 99

Nugus M, Blenkinsop T, McLeod T, Doyle M, Kent M (2005b) Structural control of gold mineralisation by reactivation of backthrusts at Sunrise Dam Gold Mine, Yilgarn Craton, WA. In: Hancock H et al (eds) Best practice and innovation in global mine geology, 29 May–3 June. Publication 64. Economic Geology Research Unit, School of Earth Sciences, James Cook University, Townsville, Queensland, p 99

Oberthür T, Weiser T, Amanor JA, Chryssoulis SL (1997) Mineralogical siting and distribution of gold in quartz veins and sulfide ores of the Ashanti mine and other deposits in the Ashanti belt of Ghana: genetic implications. Miner Depos 32:2–15

Pals DW, Spry PG (2003) Telluride mineralogy of the low-sulfidation epithermal Emperor gold deposit, Vatukoula, Fiji. Mineral Petrol 79:285–307

Pals DW, Spry PG, Chryssoulis S (2003) Invisible gold and tellurium in arsenic-rich pyrite from the Emperor Gold Deposit, Fiji: implications for gold distribution and deposition. Econ Geol 98:479–493

Pokrovski GS, Kara S, Roux J (2002) Stability and solubility of arsenopyrite, FeAsS, in crustal fluids. Geochim Cosmochim Acta 66:2361–2378

Putnis A (2002) Mineral replacement reactions: from macroscopic observations to microscopic mechanisms. Mineral Mag 66:689–708

Reich M, Kesler SE, Utsunomiya S, Palenik CS, Chryssoulis S, Ewing RC (2005) Solubility of gold in arsenian pyrite. Geochim Cosmochim Acta 69:2781–2796

Salier BP, Groves DI, McNaughton NJ, Fletcher IR (2005) Geochronological and stable isotope evidence for widespread gold mineralization from a deep-seated fluid source at ca. 2.65 Ga in

the Laverton Gold Province, Western Australia. Econ Geol 100:1363–1388

Shackleton JM, Spry PG, Bateman R (2003) Telluride mineralogy of the Golden Mile deposit, Kalgoorlie, Western Australia. Can Mineral 41:1503–1524

Sibson RH, Robert FA, Poulsen KH (1988) High-angle reverse faults, fluid-pressure cycling, and mesothermal gold-quartz deposits. Geology 16:551–555

Simon G, Huang H, Penner-Hahn JE, Kesper SE, Kao LS (1999a) Oxidation state of gold and arsenic in gold-bearing arsenian pyrite. Am Mineral 84:1071–1079

Simon G, Kesler SE, Chryssoulis S (1999b) Geochemistry and textures of gold-bearing arsenian pyrite, Twin Creeks, Nevada: implications for deposition of gold in Carlin-type deposits. Econ Geol 94:405–422

Sung Y-H, Ciobanu CL, Pring A, Brugger J, Skinner W, Cook NJ, Nugus M (2007) Tellurides from Sunrise Dam gold deposit, Yilgarn Craton, Western Australia: a new occurrence of nagyágite. Mineral Petrol 91:249–270

Tarnocai CA, Hattori K, Cabri LJ (1997) "Invisible" gold in sulfides from the Campbell mine, Red Lake greenstone belt, Ontario: evidence for mineralization during the peak of metamorphism. Can Mineral 35:805–815

Tenailleau C, Pring A, Etschmann B, Brugger J, Grguric B, Putnis A (2006) Transformation of pentlandite to violarite under mild hydrothermal conditions. Am Mineral 91:706–709

Thébaud N, Philippot P, Rey P, Brugger J, Van Kranendonk M, Grassineau N (2008) Polyphased fluid–rock interaction in the mid-Archaean and implication of gold pre-concentration: example from the Warrawoona Syncline (WA). Earth Planet Sci Lett 272:639–655

Vaughan JP (2004) The process mineralogy of gold: the classification of ore types. JOM 56:46–48

Vaughan JP, Kyin A (2004) Refractory gold ores in Archaean greenstones, Western Australia: mineralogy, gold paragenesis, metallurgical characterization and classification. Mineral Mag 68:255–277

Wu X, Deldove F (1989) Hydrothermal synthesis of gold-bearing arsenopyrite. Econ Geol 84:2029–2032

Xia F, Zhou J, Brugger J, Ngthai Y, O'Neill B, Chen G, Pring A (2008) A novel route to synthesize complex metal sulfides: hydrothermal coupled dissolution-reprecipitation reactions. Chem Mater 20:2809–2817

Xia F, Brugger J, Chen G, Ngothai Y, O'Neill B, Punis A, Pring A (2009) Mechanism and kinetics of pseudomorphic mineral replacement reactions: a case study of the replacement of pentlandite by violarite. Geochim Cosmochim Acta 73:1945–1969. doi:10.1016/j.gca.2009.01.007

Yang S, Blum N, Rahders E, Zhang Z (1998) The nature of invisible gold in sulfides from the Xianxi Au–Sb–W ore deposits in northwestern Hunan, People's Republic of China. Can Mineral 36:1361–1372